Research Square

Preprints are preliminary reports that have not undergone peer review.
They should not be considered conclusive, used to inform clinical practice,
or referenced by the media as validated information.

Obesity remodels the testicular microenvironment: Spatial transcriptomics identifies local IGF dysregulation associated with spermatogenic failure

Yan Li
Academy of Military Medical Sciences
Ting Zhao
Guangzhou Medical University
Deyi Wu
China Agricultural University
Yiming Yuan
Academy of Military Medical Sciences
Juanjuan Lang
Nanhu Laboratory
Rui Zhang
Nanhu Laboratory
Shanshan Song
Nanhu Laboratory
Junsen Hua
Nanhu Laboratory
Keren Cheng
Zhejiang University
Yuwen Ke
China Agricultural University
Kun Yu Yu
China Agricultural University
Shoulong Deng
China Agricultural University
Zhang Yi
Panzhihua University
Yefeng Qiu
qiuyefeng2001@163.com

Academy of Military Medical Sciences

Research Article

Keywords: Obesity, Testis, Spatial transcriptomics, Spermatogenesis, IGF signaling, IGFBP7

Posted Date: November 18th, 2026

DOI: https://doi.org/10.21203/rs.3.rs-11547923/v1

License: This work is licensed under a Creative Commons Attribution 4.0 International License.
Read Full License

Additional Declarations: No competing interests reported.

Obesity remodels the testicular microenvironment: Spatial transcriptomics identifies local IGF dysregulation associated with spermatogenic failure

Yan Li[1]*, Ting Zhao[2,5]*, Deyi Wu[3]*, Yiming Yuan[1]*, Juanjuan Lang[6], Rui Zhang[6], Shanshan Song[6], Junsen Hua[6], Keren Cheng[7], Yuwen Ke[5], Kun Yu[3, 4†], Shoulong Deng[3, 4†], Yi Zhang[8†], Yefeng Qiu[1†]

[1] Academy of Military Medical Sciences, Academy of Military Sciences, Beijing 100071, China

[2] Guangzhou Women and Children's Medical Center, Guangzhou Medical University, Guangzhou 510623, China.

[3] Beijing Key Laboratory for Animal Genetic Improvement, National Engineering Laboratory for Animal Breeding, Key Laboratory of Animal Genetics and Breeding of the Ministry of Agriculture, National Research Facility for Phenotypic and Genotypic Analysis of Model Animals (Beijing), College of Animal Science and Technology, China Agricultural University, Beijing 100193, China.

[4] National Science Center for Model Animals, China Agricultural University, Beijing 100193, China

[5] State Key Laboratory of Animal Biotech Breeding, China Agricultural University, Beijing 100193, China

[6] Nanhu Laboratory, Jiaxing 314000, China

[7] Department of Obstetrics and Gynecology, Center for Reproductive Medicine, the Fourth Affiliated Hospital of School of Medicine, and International School of Medicine, International Institutes of Medicine, Zhejiang University, Yiwu 322000, China.

[8] Department of Medicine, Panzhihua University, Sichuan 617000, China

* These authors contributed equally to this work.

† Correspondence: Kun Yu (yukun@cau.edu.cn); Shoulong Deng (dengsl@cau.edu.cn); Yi Zhang (zhangyi@pzhu.edu.cn); Yefeng Qiu (qiuyefeng2001@163.com).

Running title: Obesity and the testicular microenvironment

Abstract

Background: Obesity is a global metabolic disorder strongly associated with male infertility, but the spatial and molecular mechanisms underlying testicular dysfunction remain unclear.

Methods: We combined single-cell and high-definition spatial transcriptomics to construct an integrated spatial atlas of the cynomolgus monkey testis in both normal and obese conditions.

Results: This approach revealed a previously unrecognized spatial misdirection of insulin-like growth factor (IGF) signaling in the obese testicular microenvironment. Obesity was associated with a compartmentalized up-regulation of IGF1, IGFBP5, and IGFBP7 specifically within macrophages and peritubular myoid cells surrounding the seminiferous tubules. Concurrently, the IGF1 receptor and IGF2 receptor were enriched in adjacent somatic cells, suggesting a localized autocrine and paracrine signaling hub. These spatially restricted IGF-associated changes accompanied macrophage expansion and inflammatory polarization, increased myoid cell abundance, and basement membrane remodeling. The ensuing chronic inflammatory niche directly correlated with down-regulation of blood-testis barrier genes including CLDN11 and TJP1, with protein-level validation for CLDN11 and GATA4. Spermatogenesis was broadly impaired, with stage-specific transcriptional programs attenuated across the germline and ferroptosis-related gene set scores selectively increased in spermatogonia.

Conclusions: Our findings link spatially compartmentalized IGF dysregulation to testicular inflammation and spermatogenic impairment in obesity, highlighting IGF1, IGFBP5, and IGFBP7 as candidate mediators and providing a molecular basis for future research on obesity-associated male reproductive dysfunction.

Keywords: Obesity; Testis; Spatial transcriptomics; Spermatogenesis; IGF signaling; IGFBP7

Background

Obesity has been a pandemic health issue, promoting obesity-associated diseases to a burden on humans. The global rates of overweight and obesity rose continuously during 1990-2021, with the prevalence of obesity among males increasing by 155.1% since 1990. It is predicted that the number of overweight and obese people worldwide will reach 3.80 billion adults by 2050[1]. Obesity is characterized by body fat accumulating excessively or distributing in an abnormal pattern[2]. Previous literature has reviewed that more than 20 diseases, such as diabetes, asthma and myocardial infarction, are correlated with obesity. The estimated incidence of complex multiple diseases is 8.3% among elderly populations with obesity, whereas it is only 1.0% in non-obese populations[3].

Male reproductive health is a serious public health issue for humans. The seminiferous tubules within the testes serve as the primary site for spermatogenesis[4]. Spermatogonial stem cells differentiate into mature sperm through a complex and precise process involving spermatogonia differentiation, meiosis and round spermatids elongation. The spermatogenesis is also modulated by somatic cells (Sertoli cells, Leydig cells, Endothelial cells, Myoid cells) through multiple signaling pathways interacting with germ cells[5, 6]. A research for the relationship between body mass index (BMI) and semen parameters in 166 men (including 38 with severe obesity) found that BMI was negatively correlated with sperm concentration, total count, progressive motility, and normal morphology. Further, the levels of sex hormone-binding globulin (SHBG), anti-Müllerian hormone (AMH) and inhibin B were declined as BMI increased[7]. Additionally, Nguyen et al. revealed that male partner with overweight and obesity increased the risk of infertility in the study of 26,303 couples after excluding confounding factors, including female partner's age and BMI,

intercourse frequency, and smoking habits of both partners[8]. Therefore, obesity involves potential risks for spermatogenic dysfunction and infertility.

ScRNA-seq analysis unveiled that after 45 years old, spermatogenesis capacity weakened dramatically in men with high BMI (≥30), mainly due to obesity disrupted cellular metabolism, exacerbated inflammatory levels and declined sertoli-spermatogenic cells communication [9, 10]. However, the effects of obesity on spermatogenesis remain poorly understood in terms of spatial structural variations in testicular niche. Spatial transcriptomics (ST) capture gene expression profiles directly within their native tissue landscape, providing deep insights into the spatial distribution of heterogeneous cells and the spatial patterns of gene expression in different tissues[11]. Additionally, it is tough to obtain testes from healthy individuals, and non-human primates (NHP) exhibit genomes and spermatogenesis processes highly similar to those in humans[12]. Thus, NHP is an ideal model for spermatogenesis study. Herein, we revealed the molecular mechanisms underlying obesity-induced spermatogenesis dysfunction at the spatial level through combined single-cell transcriptomics and spatial transcriptomics analysis. In the current study, we applied an integrated single-cell and spatial transcriptomic approach to systematically characterize the impact of obesity on the testicular microenvironment in cynomolgus monkeys. We found that obesity was associated with a pronounced inflammatory response localized to the basement membrane region of the seminiferous tubules, accompanied by abnormal accumulation and spatial redistribution of immune, myoid and endothelial cells. Notably, obesity was linked to elevated expression of insulin-like growth factor (IGF) family genes within these regions, suggesting a potential role of dysregulated IGF signaling in driving local inflammation. Furthermore, genes essential for maintaining blood–testis barrier integrity were markedly downregulated, indicating that obesity disrupts the blood–testis barrier. Collectively, these findings reveal that obesity induces profound spatial remodeling of the testicular niche, characterized by inflammation at the basement membrane, IGF-associated

signaling alterations, and blood–testis barrier disruption, thereby providing novel insights into the mechanisms underlying obesity-associated male reproductive dysfunction.

Methods

Fabrication and assembly of microfluidic devices

Polydimethylsiloxane (PDMS) microfluidic chips were purchased from ZhongXinQiHeng (Suzhou CChip Scientific Instrument Co., Ltd.). Each chip contained 96 channels with widths of 20 μm. The photoresist thickness was approximately 20 μm for devices containing 20 μm-wide channels.

Animals

Six 10-year-old male cynomolgus monkeys (Macaca fascicularis), including three animals with obesity and three animals with a normal phenotype, were included in this study. All animal procedures were reviewed and approved by the Institutional Animal Care and Use Committee of the Laboratory Animal Center, Nanhu Laboratory (approval no. IACUC-DWZX-2024-051; approval date: 4 January 2025). All experiments were performed in accordance with the approved protocol and relevant institutional guidelines and regulations for the care and use of laboratory animals. The study is reported in accordance with the ARRIVE 2.0 guidelines.

Tissue preparation and embedding

Testes of cynomolgus monkeys from the normal and obese groups were collected. Following dissociation, fresh tissue was placed into cryomolds and embedded with chilled optimal cutting temperature (OCT) compound, avoiding bubble formation. The cryomolds containing tissue and OCT were immediately placed on powdered dry ice until the OCT was fully solidified. The frozen tissue blocks were then either processed for cryosectioning or stored at −80 °C for long-term preservation.

Preparation of poly-L-lysine coated slides

Poly-L-lysine coated slides (84.9 × 46.54 × 1 mm) were provided by Jiangsu Shitai Laboratory Equipment Co., Ltd. These slides were directly used for subsequent experiments without additional surface treatment.

Tissue cryosection

Prior to sectioning, frozen tissue blocks were equilibrated in the cryostat chamber at −20 °C. The blocks were sectioned at a thickness of approximately 10 μm, suitable for use with 20 μm-wide PDMS channel devices. The tissue sections were mounteded at the center of custom poly-L-lysine coated glass slides designed for the 96-channel PDMS chips. Prepared slides were stored at −80 °C until further use.

Hematoxylin and eosin (HE) staining

Briefly, after dewaxing and rehydration, the testicular tissue sections (5-μm thickness) embedded in paraffin were stained by hematoxylin and eosin according to the manufacturer's instruction (Servicebio, G1005).

Immunofluorescence staining

Consistent with the previous description, paraffin-embedded testicular tissue sections (5-μm thickness) were deparaffinized and rehydrated. Followed by antigen repair for 30min, 3%BSA was used to block the sections. After washing with PBS (pH7.4), the sections were incubated with the prepared primary antibody at 4℃ overnight in a wet box. Next, the sections were rinsed and incubated with the corresponding fluorescence-labeled secondary antibody at RT for 50min in the dark. After incubation, Hoechst 33342 (Thermo Fisher, H3570, 1:1000) was applied for counterstaining nuclei. The sections were mounted in coverslips with anti-fade mounting medium. Leica Aperio Versa200 was used for the fluorescent image capture. The antibodies used for immunofluorescence staining are as follows: Claudin11(Thermo Fisher, 36-4500, 1:200), CD80

(Novus biological, NBP2-02905, 1:200), IGF1 (abcam, ab9572, 1:200), IGFBP5 (Novus biological, NBP2-68755, 1:200), IGFBP7 (abcam, ab171085, 1:200), Goat Anti-Rabbit Alexa Fluor 647 (abcam, ab150079), Goat Anti-Rabbit Alexa Fluor 488 (abcam, ab150077).

Immunohistochemistry staining

Paraffin-embedded testicular tissue sections were sectioned into 5-μm-thick slices, which then were deparaffinized and rehydrated using a graded ethanol series (100%, 100%, 95%, 80%, 75%). For antigen retrieval, the sections were boiled in citrate buffer (pH 6.0) and then cooled naturally. Endogenous peroxidase activity was quenched by incubation with 3% H_2O_2. After blocking with 3% BSA, the sections were incubated overnight at 4°C with the primary antibody. Subsequently, the sections were incubated with an HRP-conjugated secondary antibody followed by development with DAB substrate. The cell nuclei were counterstained with hematoxylin. Finally, the sections were dehydrated, cleared in a series of graded alcohols and xylene, and mounted with the neutral resinous mounting medium. Images were scanned by Leica Aperio Versa200. The antibodies used for immunohistochemistry staining are as follows: GATA4 (abcam, ab227512, 1:200).

Single-cell RNA-seq sequencing

With the use of a Chromium Single Cell 3' GEM, Library & Gel Bead Kit v3.1 (10x Genomics, PN-1000268), the SIC single-cell suspension (700-1200 living cells per ml as determined by the CellDrop FL Cell Counter) was loaded onto a Chromium Single Cell Chip (Chromium Single Cell G Chip Kit, 10x Genomics, PN-1000120) according to the manufacturer's instructions, for co-encapsulation with barcoded Gel Beads at a target capture rate of 6,000 individual cells per sample. We lysed captured cells and released RNA was barcoded through reverse-transcription in individual single-cell gel beads in the emulsion (GEMS). In each droplet, complementary DNA (cDNA) was generated and amplified through reverse-transcription on a T100 PCR Thermal

Cycler (Bio Rad) at 53 °C for 45 min, followed by 85 °C for 5 min and a hold at 4 °C. Then, cDNA concentration and quality were assessed using Qubit Fluorometer (Thermo Scientific) and bioanalyzer 2100 (Agilent), respectively. According to the manufacturer's instructions, scRNA-seq libraries were constructed and sequenced to a depth of 40,000 reads per cell on illumina platform by Annoroad Gene Technology Co., Ltd.

Pre-processing and quality control of scRNA-seq data

Raw data generated by the NovaXplus sequencing platform were first processed using bcl2fastq (version 2.20.0.422) to convert BCL files into FASTQ format. Next, the FASTQ reads were aligned to the pre-mRNA reference (Ensembl, Macaca_fascicularis_6_0) and counted using Cell Ranger (version 7.2.0) (10× Genomics) with the default parameters. CellBender (version 0.3.2) was applied to the count matrix of each sample to remove the contamination of background mRNA. The filtered matrixes were further analyzed with Seurat (version 5.3.0). Cells with genes range from 200 to 7000, total counts range from 1000 to 50000, mitochondrial genes ratio lower than 5% were kept. DoubletFinder (version 2.0.6) was used to detect and remove doublets. After integration and clustering, clusters lacking specific marker genes, dominating in one sample, and with relatively low gene content or high mitochondrial ratio were also discarded.

Sample integration, clustering, and annotation of cell types

Data normalization, integration, dimensionality reduction, clustering, and differential gene expression analysis were performed under the corresponding pipeline of Seurat packages (version 5.3.0). The filtered count matrix of each sample was normalized using the "SCTransform" function. Principal component analysis and batch correction were performed using the "RunPCA" and "RunHarmony" functions, respectively. After data integration and scaling, the first 50 PCs were used to execute the dimensionality reduction with the "RunTSNE", "RunUMAP" and "FindNeighbors" functions. Clustering was performed using the "FindClusters" function with the

resolution of 0.3. Next, primary and secondary cell types were identified according to the expression levels of reported marker genes in testicular cells of Macaca fascicularis[13]. After cell type identification, the marker genes of each cell type were calculated using the "FindAllMarkers" function with default parameters. The top marker genes for each cell type are shown in Table S1.

Spatial transcriptome library preparation

Based on the DBiT-seq (deterministic barcoding in tissue for spatial omics sequencing) method, high-definition spatial RNA-seq (hdST-seq) libraries were constructed for testis samples from normal and obesity cynomolgus monkeys. Three samples were collected from the normal group and three samples from the obese group. Polydimethylsiloxane microfluidic chips with 50 20-μm-wide channels and 96 10/20-μm-wide channels were obtained from a commercial source, ZhongXinQiHeng (Suzhou CChip Scientific Instrument). The detailed procedures are provided in the supplemental materials and methods. All oligonucleotides used are listed in Table S2.

Pre-processing and quality control of spatial transcriptomic data

To generate gene expression matrices for each sample, we first utilized the UMI-tools (version 1.1.6) to extract the Barcode B, Barcode A, and UMI in Read2. We then used the ST pipeline (version 1.8.1) with default parameters to process these reformatted fastq files. This involved adapter trimming, read alignment to the reference genome (Ensembl, Macaca_fascicularis_6_0), cell barcode demultiplexing, read annotation (Ensembl, Macaca_fascicularis_6_0), and UMI counting. During the read annotation, intronic reads from nascent RNA transcripts present in the nuclei were retrieved by extending the CDS regions to the whole transcript regions, and the final matrix was generated from the combination of exonic reads and intronic reads. To ensure that only pixels within the tissue slice were analyzed, we manually aligned adjacent H&E staining with the spatial pixel map according to their boundaries, and extracted the coordinates of valid pixels within the tissue.

Spatial transcriptomic data integration, deconvolution, and niches clustering

We processed and analyzed the pixel-by-gene count matrix obtained from each sample using Seurat packages. High-quality pixels with genes greater than 100, detected UMIs greater than 100 were kept. Next, each sample was individually normalized using regularized negative binomial regression with "SCTransform" function. Since there was no evidence of batch effect between different replicates and different channels (10 μm & 20 μm), we combined pixels from each sample using the "merge" function directly. This allowed us to obtain the normal Macaca fascicularis testis map and obesity Macaca fascicularis testis map, respectively. For each combined dataset, we used the intersected variable genes from individual samples to serve as the set of variable genes for downstream analysis. For the annotation of spots, the RCTD deconvolution method from spacexr package (version 2.2.1) was applied to calculate the proportions of various cell types in each spot. Then, the majority voting algorithm was used to identify the primary and secondary of spots. Based on the spot cell type composition matrix, the cellular niche of each sample was identified using the k-means clustering algorithm of ISCHIA package (version 1.0.0.0). We also perform the molecular niches analysis based on the count matrix of gene expression by using the Louvain algorithm via the "FindClusters" function with the resolution of 0.6, after the dimensionality reduction with the "RunPCA", "RunUMAP" and "FindNeighbors" functions.

Spatial co-localization analysis

We used MISTy implementation in mistyR (version 1.16.0) to estimate the importance of the abundance of each major cell type in explaining the abundance of the other major cell types. Cell-type RCTD estimations of all slides were modelled in a multi-view model using two different spatial contexts: (1) an intrinsic view that measures the relationships between the deconvolution estimations within a spot, and (2) a juxta view that sums the observed deconvolution estimations

of immediate neighbours (largest distance threshold = 6). The aggregated estimated standardized importances (median) of each view of all slides were interpreted as celltype dependencies in different spatial contexts, such as colocalization or mutual exclusion. Next, we used the nearest neighbour search algorithm in RANN (version 2.6.2) package to calculate the proportions and distances of their nearest neighbour cells in space.

Differentially expressed genes analysis

Differentially expressed genes (DEGs) of each celltype of Macaca fascicularis testis in the normal group compared to those in the obesity group were analyzed by the "RunDEtest" function of SCP package (version 0.5.1) using Wilcoxon Rank Sum test, and were identified with the cutoff of average $|LogFC| > 1$ and adjusted P-values < 0.05. DEG lists for each celltype are shown in Table S3. For certain important genes expressed associated with the blood-testis barrier or steroid metabolism, even if their average $|LogFC| < 1$, we still included them as long as their adjusted p-value < 0.05. Additionally, we performed a two-tailed Student's t-test on their normalized expression values from "SCTransform" function to validate the statistical reliability.

Pathway enrichment analysis

The clusterProfiler package (version 4.16.0) was used to perform gene ontology terms (GO) and kyoto encyclopedia of genes and genomes (KEGG) enrichment analysis. Representative terms were selected with the cutoff of P-values < 0.05 and were then visualized with ggplot2 package (version 4.0.0).

Analysis of Weighted gene co-expression network and transcriptional regulatory network

We used the hdWGCNA package (version 0.4.6) to perform high-dimensional weighted gene co-expression network analysis (hdWGCNA) for spatial transcriptomic data. Initially, we set up a Seurat object for hdWGCNA by selecting genes that are expressed in at least 5% of cells in each dataset. We then construct metacells using k-Nearest Neighbors (KNN = 25) to yield a metacell

gene expression matrix. Following normalization and scaling of the data, we construct co-expression network by using default parameters. We then computed all module eigengenes (MEs) in the full spatial transcriptomic datasets, harmonized module eigengenes and computed eigengene-based connectivity (kME) for each gene. We also use the "GetModules" and "DotPlot" functions to generate the heatmaps of celltypes associated modules and used clusterProfiler to perform module specific gene ontology enrichment. We continued to use the "ModuleNetworkPlot" function to visualize the network underlying the top 25 hub genes for each module. Additionally, we used the topological overlap matrix (TOM: one type of weighted correlation matrix) generated during the hdWGCNA processes for the assessment of gene-gene interaction. The weak correlations of values in the topological overlap matrix less than 0.01 were eliminated for avoiding the appearance of the spurious correlation. The construction of transcriptional regulatory network was performed using the TF analysis workflow with default parameters in hdWGCNA. Transcription factors (TFs) stored in JASPAR 2020 database were downloaded as reference TFs for downstream analysis. After the motif scan with the "MotifScan" function, the transcriptional regulatory network was constructed by using the XGBoost algorithm in the "ConstructTFNetwork" function. Next, we use the "FindDifferentialRegulons" function to identify the TFs with different regulatory effects (positive or negative) during the comparison between normal and obesity testis samples. These TFs were further used to construct the module regulatory network, and visualized by the functions of "ModuleRegulatoryHeatmap" and "ModuleRegulatoryNetworkPlot".

Pseudotime analysis

Pseudotime analysis was performed on spermatogenic cells of scRNA-seq data with the Monocle2 package (version 2.36.0). We used the "newCellDataSet" function with the "lowerDetectionLimit" parameter of 0.1 to transform the Seurat objects as the CellDataSet objects for downstream

analysis. Then, we used the function "detectGenes" to filter out low-quality genes that are expressed in very few cells (less than 10 cells). DEGs between celltypes were identified by the "differentialGeneTest" function of Monocle2 with the cutoff of q-value < 0.01. The top 3,000 DEGs were selected for the DDRTree dimensional reduction to project the pseudotime trajectory of spermatogenic cells. The cells described above were ordered according to pseudotime. Further, we used the "plot_pseudotime_heatmap2" function in ClusterGVis package (version 0.1.4) to plot a pseudotime-ordered heatmap and classify the DEGs along the pseudotime trajectory as 5 clusters. We then used the "AddModuleScore" function of Seurat to calculate the scores of each cluster in cells. Based on the results of pseudotime analysis from Monocle2, we used CytoTRACE2 package (version 1.1.0) to calculate the developmental potential scores of spermatogenic cells and compared the difference between groups using two-tailed Student's t-test.

Gene set score analysis

The canonical pathways of spermatogenesis and cell death were obtained from GO, KEGG, and MSigDB database. The "scgsva" function in scGSVA package (version 0.0.23) was used for calculate the pathway gene set scores. Cell differentiation related gene sets were obtained from the pseudotime analysis described in the previous section of pseudotime analysis. The gene set used for macrophage polarization scoring comprises classical polarization markers and hallmark inflammatory factor genes. These gene sets were then used for scoring each input cell with the "AddModuleScore" function of Seurat based on gene expression level. Alternations in the scores of the normal group compared to the obesity group were analyzed via ggplot2 package using two-tailed Student's t-test.

Cell-cell communication analysis

Cell–cell communication was inferred through CellChat package (version 2.2.0). The CellChatDB.human database was specifically chosen for this analysis. The expression matrix

served as the input for CellChat using default settings (type = triMean, min.cells = 10). After this, we extracted cell–cell communication counts and weights and the inferred cell–cell communication through the "netVisual_circle", "netVisual_heatmap", and "netVisual_aggregate" functions. To visualize the differential number of interactions or interaction strength across distinct cell populations, comparison of interaction counts and weights between groups were conducted and visualized using the functions of "rankNet", "netAnalysis_signalingRole_scatter", "netAnalysis_signalingRole_heatmap", and "netAnalysis_signalingChanges_scatter".

Assessment of the ratio of observed over expected numbers

To characterize the distribution of meta-clusters, the ratio of observed over expected numbers (Ro/e) were calculated and used to indicate preferences by using a reported method. Specifically, for each combination of meta-cluster i and group j, a 2 by 2 contingency table was constructed, which contained the number of cells or spots of meta-cluster i in group j, the number of cells or spots of meta-cluster i in other groups, the number of cells or spots of non-i meta-clusters in group j, the number of cells or spots of non-i meta-clusters in other groups. Then, we used these value to calculate the observed number of cells or spots of meta-cluster i in group j, and the expected number of cells or spots of meta-cluster i in group j. Finally, Ro/e equals the observed values divided by the expected values. The symbols of results represents different preferences. The symbol "++" means the specific meta-cluster i is highly enriched in group j with Ro/e > 1.2; the symbol "+" means the specific meta-cluster i is moderately enriched in group j with 1.2 >= Ro/e > 1; the symbol "+/-" means the specific meta-cluster i is slightly depleted in group j 1 >= Ro/e > 0.5; the symbol "-" means the specific meta-cluster i is depleted in group j Ro/e <= 0.5.

Copy number variations analysis

The copy number variations (CNVs) of cells or spots was calculated with infercnv package (version 1.24.0), which analyzes gene expression intensity across the genome based on scRNA-

seq or spatial transcriptomic data. Cells or spots in normal group were selected as the references. The CNVs analysis was performed with parameters including “denoise”, a value of 0.1 for “cutoff”, and other default settings. A heatmap was generated to illustrate the relative expression intensities across each chromosome.

Statistical analysis

All experimental data were statistically analyzed using R stats package (version 4.5.1). Results were presented as mean ± SEM. Comparisons were conducted using the two-tailed Student’s t-test two-sided Wilcoxon Rank Sum test, or one-way ANOVA as indicated in figure legends. P-values are presented in indicated figures.

Use of large language models

During manuscript preparation, the authors used ChatGPT (OpenAI) solely for English-language editing and formatting assistance. All output was reviewed and revised by the authors, who take full responsibility for the content of the manuscript.

Results

Obesity-induced impairment of semen quality and associated reproductive functions

The comparative analysis revealed obesity-associated alterations in semen parameters and specific reproductive hormones. As detailed in Table 1, subjects in the obese group demonstrated profoundly impaired semen quality compared to the normal group. Key parameters including sperm survival rate, motility, concentration, and all kinematic measures (VCL, VSL, LIN, STR, VAP, ALH, WOB) were significantly reduced ($p<0.05$). Hormonal profiling (Table 2) indicated selective dysregulation, with the obese group exhibiting significantly elevated levels of estradiol (E2, $p=0.044$) and adiponectin (ADI, $p=0.004$). In contrast, no statistically significant differences were observed in the levels of the immune factors analyzed (IFN-γ, IL-10, IL-4, IL-1β, TNF-α, IL-

6, IL-12A, VEGFA, TGFB1) between the two groups (Table 3, $p>0.05$). These results collectively indicate that obesity is associated with a severe decline in semen quality and specific endocrine disturbances, without significant changes in the panel of immune factors examined.

Establishment of a spatial transcriptomic atlas of normal and obese cynomolgus monkey testes with cell-type decomposition of scRNA-seq data

To delineate the testicular microenvironment in obesity at single-cell resolution, we constructed an integrative multi-omics atlas by combining single-cell RNA sequencing (scRNA-seq) and high-definition spatial transcriptomics (ST) of cynomolgus monkey testes (Fig. 1A). Initial analysis of 31,156 high-quality cells (14,967 from normal and 16,189 from obese individuals) identified 11 major testicular populations (Fig. 1B). Uniform manifold approximation and projection (UMAP) visualization, anchored by marker expression (Fig. 1C), defined spermatogonia (SPGs; NANOS3+, KIT+), spermatocytes (SPCs; SPATA22+, AURKA+), round spermatids (Round; ACRV1+, NME5+), elongating spermatids (Elongating; TNP2+, PRSS37+), elongated spermatids (Elongated; OAZ3+, PRM2+), Sertoli cells (Sertoli; SOX9+, CLDN11+), macrophages (Macrophage; C1QA+, CD14+), myoid cells (Myoid; ACTA2+, MYH11+), Leydig cells (LCs; PDGFRA+, AR+), immature Leydig cells (ILCs; FLT4+, CYP26B1+), and endothelial cells (Endothelial; CD34+, COL1A1+). High-resolution sub-clustering further resolved the developmental continuum of spermatogenesis (Supplementary Fig. S1A). Within the germline, we identified a total of 20 sub cell-types, including 2 undifferentiated (Undiff1/2) and 3 differentiating (Diff1-3) spermatogonia, sequential 5 meiotic stages (Dip & Sec. Spcs: Diplotene and secondary spermatocytes; Zyg: Zygotene; Pach1-3: pachynema 1-3), 10 spermatid substages, comprising round spermatids (RS1-4; RS_ex: extraordinary round spermatids) and elongating spermatids (ES1-5). Gene Ontology enrichment confirmed their functional identities (Supplementary Fig. S1B).

Spatial transcriptomics profiling generated 52,744 high-confidence tissue spots (25,670 from normal and 27,074 from obese individuals). Employing the Robust Cell Type Decomposition (RCTD) algorithm with our comprehensive scRNA-seq atlas (including major types and sub-states) as a reference, we deconvoluted the cellular composition of each spot. This analysis successfully mapped both major cell-types populations and fine-grained sub cell-types onto the testicular architecture. The resulting spatial maps accurately reconstructed the seminiferous tubule organization, visualizing the orderly, stage-specific progression of germ cells and the spatial distribution of somatic niches (Fig. 1D-F; Supplementary Fig. S1C, D). This integrated atlas establishes a foundational, high-resolution spatial resource for investigating obesity-induced remodeling of testicular cellular ecology.

Obesity-induced remodeling of testicular cellular signatures

Obesity induced a significant remodeling of the testicular cellular composition and spatial organization. Analysis of major cell-types using spatial transcriptomics revealed a marked depletion of round spermatids ($p=0.002$) alongside a significant expansion of somatic populations, including macrophages ($p=0.02$), Myoid cells ($p=0.03$), and endothelial cells ($p=0.01$) in obese testes (Fig. 2A, B). The Ratio of Observed over Expected numbers (Ro/e) further indicated a global shift, with depletion of germ cell types like round spermatids and enrichment of somatic cells such as macrophages (Fig. 2C). Sub-cell-type analysis identified the subtypes RS_ex, RS_1 and RS_2 as the primary drivers of round spermatid loss (Supplementary Fig. S2A, C; $p<0.05$). Although there was no difference in the major cell population of spermatogonia, we noted a proportional increase in the differentiating Diff3 spermatogonial subset (Supplementary Fig. S2A, C; $p=0.03$) and the Undiff2 progenitor population (Supplementary Fig. S2A, C; $p=0.03$). Ro/e analysis revealed a similar trend in cellular proportion changes (Supplementary Fig. S2B). HE stained sections of testicular tissues further demonstrated that the seminiferous tubules in the

obese group exhibited significant atrophy of the adluminal compartment, a drastic decrease in spermatogenic cells, and thickening of the basement membrane (Fig. 2D).

Spatial niche analysis, defined by both cellular composition (CC clusters) and transcriptional profiles (Molecular clusters), demonstrated a concomitant reorganization of the tissue architecture. Specific cell niches, most notably CC2, CC10, CC11, and molecular niches, like Cluster_2, Cluster_6, Cluster_8, were substantially expanded in obesity (Fig. 2E, F). These expanded niches were predominantly composed of macrophages, Myoid and endothelial cells (Fig. 2G). Conversely, niches enriched for spermatogenic cells, including spermatogonia (SPGs) and round spermatids—such as the cellular niches CC4, CC5, and CC8 and the molecular niches Cluster_1, Cluster_3, and Cluster_7—exhibited a pronounced reduction (Fig. 2E-G). These spatial niche alterations were consistent with the previously observed changes in cellular proportions. Together, the results delineate a multi-level restructuring in obese testes, encompassing shifts in specific cellular sub populations and a profound reorganization of their spatial niches within the testicular micro-environment.

Spatial transcriptomics reveals the colocalization changes between macrophages and seminiferous tubule cells

Spatial co-localization analysis demonstrated significant alterations in macrophage distribution and interaction within obese testes. The minimum distance between macrophages and other major testicular cell types, including endothelial cells, Leydig cells, myoid cells, Sertoli cells, round spermatids, elongating spermatids, SPCs, and SPGs, was markedly reduced in obesity (Fig. 3A; $p<0.05$). Using a multi-view spatial dependency model (MISTy), we quantified cell-type inter-dependencies at two spatial scales: within individual spots (intrinsic view) and among immediate neighboring spots (juxta view). The analysis revealed significantly elevated importance values for macrophage-centered interactions in both views under obesity ($p<0.05$), indicating enhanced

spatial co-localization and dependency between macrophages and surrounding seminiferous tubule cells (Fig. 3B). These changes were accompanied by a pronounced redistribution of macrophages toward the seminiferous tubule basement membrane (STBM) (Fig. 3C), as visualized in spatial feature plots (Fig. 3D). Collectively, the data revealed a remodeled macrophage niche in obese testes, characterized by closer physical proximity and strengthened spatial dependencies with germ and somatic cells, particularly along the tubule periphery.

Macrophage polarization and alterations in cell-cell communication

Spatial transcriptomic analysis revealed a pronounced shift in the functional phenotype of testicular macrophages under obesity conditions. Assessment of macrophage polarization demonstrated elevated levels of both M1 (pro-inflammatory) and M2 (anti-inflammatory) polarization scores in the obese group, which manifested as a distribution within a higher numerical range compared to normal controls (Supplementary Fig. S3A). This pattern of increase was similarly observed in the gene set scoring of core pro-inflammatory (PF) and anti-inflammatory (AF) factors within macrophages, with both factors showing higher score distributions in the obese cohort (Supplementary Fig. S3B). Spatial visualization of macrophage sub-types illustrated an accumulation of M1+ and M2+ macrophages in obese testes, particularly localized near the seminiferous tubule basement membrane (STBM), contrasting with their more dispersed distribution in normal tissue (Fig. 4A).

In addition to macrophage-specific changes, tissue-wide inflammatory scoring revealed a significantly heightened inflammatory tone in obese testes, as reflected in elevated PF scores across all cell types (Supplementary Fig. S3C; Fig. 4C, D). Spatial classification of inflammatory regions identified expanded pro-inflammatory zones (PF+AF-and PF+AF+) in obese samples, which were predominantly localized to the STBM region (Fig. 4B). Cellular characterization of these inflammatory hotspots indicated that spots within PF+ regions exhibited high transcriptional

activity in myoid, endothelial cells, macrophages, and spermatogonia, with a significant increase in their abundance under obesity (Fig. 4C, D). Notably, the PF+AF-region showed a specific increase in spot counts within myoid cells and spermatogonia of obese testes, suggesting a localized pro-inflammatory milieu in the peritubular compartment (Fig. 4D). Furthermore, a modest but consistent elevation in AF values was observed in obese testicular tissues (Supplementary Fig. S3C; Fig. 4B, E), the cause of which remains undetermined but may be linked to tissue repair mechanisms following inflammatory responses.

Concurrent with these inflammatory changes, cell-cell communication networks were substantially remodeled in obese testes. Comparative analysis using CellChat indicated a global enhancement in both the number of interactions and overall interaction strength in the obese microenvironment (Fig. 5A). Macrophages emerged as central signaling hubs, demonstrating significant increases in both incoming and outgoing interaction strengths, indicative of heightened bidirectional communication (Fig. 5B). In contrast, spermatogonia, Sertoli, and endothelial cells exhibited reduced incoming interaction strength, suggesting impaired reception of microenvironmental signals in obesity (Fig. 5B). Ligand-receptor analysis identified several signaling pathways differentially active between groups. Obesity was associated with upregulated communication involving pro-inflammatory and immune-regulatory pathways, including signals mediated by CXCL, MIF, FSH, CD23, and CD86 (Fig. 5C, D). Relative information flow analysis confirmed elevated activity in pathways such as CD86 and CD23 signaling in obese testes (Fig. 5C). Conversely, pathways linked to trophic support and tissue homeostasis, including EGF and VEGF signaling, were more prominent in normal testes (Fig. 5C, D).

Further examination of adhesion-related signaling revealed nuanced changes. While ADGRL-mediated interactions were generally reduced in obesity, certain communications originating from myoid cells were preserved (Supplementary Fig. S4A-C). In contrast, interactions involving CADM1 and LAMININ were significantly increased in both quantity and intensity in obese testes,

with these interactions largely centered on macrophages and their communication with stromal cells (Supplementary Fig. S4A-C). Additionally, analysis of cytokine signaling showed that macrophages in obese testes engaged in strengthened interactions with myoid cells and spermatogonia via pro-inflammatory mediators IL1 and CSF, whereas signaling through the anti-inflammatory factor VEGF was notably attenuated (Supplementary Fig. S4C). More strikingly, under obese conditions, testicular IGF signaling shifted into highly enriched intercellular hubs among macrophages, myoid cells, endothelial cells, spermatogonia, and Leydig cells, featuring a selective exclusion of Sertoli-mediated cellular communications (Supplementary Fig. S4A-C).

These findings collectively illustrate that obesity induces a pro-inflammatory rewiring of the testicular microenvironment, characterized by M1-polarized macrophage accumulation at the tubule boundary, a generalized increase in communication network activity with macrophages as central nodes, and a shift in signaling toward inflammatory and adhesion-related pathways, alongside a decline in trophic and anti-inflammatory communication. This reconfigured intercellular dialogue likely contributes to the inflammatory recruitment and structural alterations observed within the obese testicular niche.

Potential disruption of blood-testis barrier (BTB) and steroid metabolism in the testis

Comprehensive analysis of spatial transcriptomic data revealed a pronounced and coordinated down-regulation of genes critical for the structural integrity of the blood-testis barrier (BTB) and for steroid hormone biosynthesis in the testis under obesity conditions.

Evaluation of BTB-associated genes demonstrated a significant reduction in their expression in obese testes compared to normal controls (Fig. 6A; $p<0.05$). Following SCTransform normalization, key BTB components, including tight junction protein 1 (TJP1), claudin 11 (CLDN11), and transcription factors GATA4 and WT1, exhibited consistently lower expression levels in the obesity group (Fig. 6A). Spatial visualization confirmed these findings, showing

markedly diminished and spatially dispersed expression patterns of CLDN11 and GATA4 in the seminiferous tubule architecture of obese samples (Fig. 6B). This transcriptional down-regulation was further validated at the protein level. Immunofluorescence staining for CLDN11 showed reduced signal intensity in obese testes, while immunohistochemistry for GATA4 similarly indicated decreased protein abundance (Fig. 6C). Supplementary Fig. S5 provides detailed resolution-specific (10-μm and 20-μm) expression patterns for a broader panel of BTB-related genes (TJP1, WT1, ACTG1, MYH10, TGFBR1, KRAS, BRAF, RAF1, MAPK1, HDAC1, HDAC7, HDAC9), collectively suggesting a widespread suppression of molecular networks essential for BTB maintenance and Sertoli cell function in the obese state.

Parallel investigation into steroidogenic capacity revealed a similar trend of transcriptional suppression. Genes encoding pivotal enzymes and regulators of steroid metabolism, such as CYP17A1 and CYP19A1, were significantly down-regulated in obese interstitial compartments (Fig. 6A; $p<0.05$). Spatial mapping of these genes illustrated a substantial decrease in their expression within the interstitial Leydig cell regions of obese testes compared to normal tissues (Fig. 6B). Supplementary Fig. S6 offers granular spatial expression data for additional steroid metabolism-related genes (CYP2E1, STARD10, HSD17B6, HSD17B12, MAPK6, AKT2), consistently demonstrating reduced expression in obesity across both spatial resolutions. This coherent down-regulation of steroidogenic pathway genes strongly suggests an impaired capacity for testosterone biosynthesis within the interstitial niche of obese testes.

In summary, the integrated data delineate a dual pathological signature in obese testes: a compromised transcriptional program for BTB integrity within the seminiferous tubules, and a deficient steroidogenic transcriptional program within the interstitial compartment. These disruptions likely contribute to the disrupted spermatogenic microenvironment and hormonal imbalance associated with obesity-induced testicular dysfunction.

Obesity-induced molecular alterations in process of spermatogenesis and cell death

Based on the integrated analysis of single-cell and spatial transcriptomic data from cynomolgus monkey testes, obesity induces profound and specific molecular alterations that disrupt spermatogenesis and activate selective cell death pathways. Pseudotime trajectory analysis delineates the continuous differentiation path of germ cells from spermatogonia (SPGs) to elongated spermatids (Fig. 7A). While the overall trajectory architecture is preserved in obese individuals, a detailed examination reveals a global attenuation of stage-specific transcriptional programs (Fig. 7A-C). Notably, obesity significantly impairs the differentiation capacity of spermatogonia, markedly reducing their developmental potential scores (Fig. 7B; $p<0.05$). Further analysis identifies five distinct gene clusters (Clusters 1-5) dynamically expressed along the pseudotime axis, each associated with specific developmental stages and functions: Cluster 1 (enriched in SPGs) with nucleosomal DNA binding; Cluster 2 (peaking in spermatocytes/SPCs) with tubulin binding; Clusters 3 & 4 (transiently expressed in round spermatids) with RNA polymerase II general transcription initiation factor activity and protein serine kinase activity, respectively; and Cluster 5 (predominant in elongating/elongated spermatids) with ubiquitin-like protein ligase activity (Fig. 7C). Critically, the expression levels of genes within all these functionally distinct clusters are markedly and consistently reduced in their respective cell types in the obese group compared to normal controls (Fig. 7D; $p<0.05$). This indicates a broad breakdown in the precise transcriptional coordination required for orderly germ cell maturation.

The functional consequences of this transcriptional dysregulation are quantitatively captured in the gene set score analysis across major (Fig. 7E) and substage-resolved (Supplementary Fig. S7) germ cell populations. A patterned, rather than uniform, down-regulation is observed, affecting specific modules across the spermatogenic lineage. Significant reductions of spermatogenesis scores are most prominent in early round spermatids (RS_ex and RS_2; Fig. 7E, S7; $p<0.05$). Mitosis is impaired specifically within the proliferative compartments, showing significant

declines in undifferentiated (Undiff1 and Undiff2; Fig. 7E, S7; $p<0.05$) , but not in differentiating (Diff1-3; Fig. 7E, S7; $p>0.05$) spermatogonia. We did not observe severe and consistent down-regulations across meiosis stages (Fig. 7E, S7; $p>0.05$). However, the defect in spermatid differentiation is phase-specific, marked by significant reductions in round spermatid subsets (RS_ex, RS2, RS4; Fig. 7E, S7; $p<0.05$). Finally, impairments in cilium organization and sperm motility—processes essential for terminal function—are spatially restricted, manifesting significantly only within specific elongating spermatid substage (ES5; Fig. 7E, S7; $p<0.05$). The coordinated decline in these essential functional modules points to a systemic failure in the molecular machinery governing germ cell proliferation, differentiation, and ultimate maturation into functional spermatozoa.

Concurrently, a highly specific pattern of cell death pathway activation emerges under obese conditions. Gene set score analysis reveals a significant upregulation of programmed cell death and regulation of programmed cell death exclusively within spermatogonia (SPGs) in the obese group (Supplementary Figs. S8 and S9; $p<0.05$). Gene set analysis indicates that this SPG-specific transcriptional signature is primarily associated with ferroptosis (Supplementary Figs. S8 and S9; $p<0.05$). By contrast, other germ cell types—including SPCs, Round, Elongating, and Elongated—show no significant activation of this particular death pathway (Supplementary Figs. S8 and S9; $p>0.05$). However, a separate, generalized stress response is evident, as the score for autophagy is significantly elevated across all these germ cell types in obesity (Supplementary Figs. S8 and S9; $p<0.05$). This delineates a critical dichotomy: the foundational spermatogonial stem and progenitor cell pool exhibits selective vulnerability to potent, lytic death pathways like ferroptosis and necrosis, while all germ cells experience a heightened state of autophagy, likely a response to the obesogenic stress. These transcriptional signatures suggest increased vulnerability of SPGs to cell death, which may contribute to reduced spermatogenic output; gene set scores alone do not establish cell death or its mechanism.

Co-expressed gene modules associated with obesity-mediated testicular damage

Our spatial transcriptomic analysis revealed profound alterations in local gene expression programs within the obese testicular microenvironment. To systematically identify and characterize these dysregulated programs, we performed high-dimensional weighted gene co-expression network analysis (hdWGCNA), which delineated 9 spatially conserved gene modules (SMs) (Fig. 8A-C). All the 9 modules were strikingly and selectively upregulated in testicular tissues from obese individuals compared to normal controls (Fig. 8A; $p<0.05$). To delineate inter-modular relationships, we first assessed correlations among co-expression modules. SM4 and SM6 exhibited a positive correlation (Spearman $r>0.05$, $p<0.05$) with each other but were negatively correlated (Spearman $r<0$, $p<0.05$) with SM5, SM7, and SM8 (Fig. 8B). Functional correlation analysis revealed that the M1-macrophage polarization score positively correlated (Spearman $r>0$, $p<0.05$) with SM4 and SM6 expression, while negatively correlating (Spearman $r<0$, $p<0.05$) with SM5, SM7, and SM8 (Fig. 8C); in contrast, the M2-polarization score was only negatively associated (Spearman $r<0$, $p<0.05$) with SM8 (Fig. 8C). Steroid metabolism score showed a positive correlation (Spearman $r>0$, $p<0.05$) with SM2 and a negative correlation (Spearman $r<0$, $p<0.05$) with SM6 (Fig. 8C). Notably, blood-testis barrier (BTB) integrity score was positively associated (Spearman $r>0$, $p<0.05$) with SM4 and SM6, yet negatively associated (Spearman $r<0$, $p<0.05$) with SM5, SM7, and SM8—a pattern seemingly contradictory to the expected barrier impairment upon SM4/SM6 overexpression (Fig. 8C). Paired-connection analysis resolved this paradox: in normal testes, SM4/SM6 expression and BTB integrity showed a positive correlation, whereas in obese testes this relationship reversed, with most samples displaying elevated SM4/SM6 alongside reduced barrier integrity (Fig. 8D), suggesting context-dependent roles of these modules. Further analysis showed the modules SM4 and SM6 were predominantly expressed in endothelial cells, macrophages, Myoid cells, and spermatogonia, which exhibited a

602 highly specific localization to the regions surrounding the seminiferous tubule basement
603 membrane (Fig. 8E, F).

604 **IGF family genes: the core of testicular injury-associated SM4/SM6 gene modules**

605 To further identify the key target genes involved in obesity-induced testicular damage, we
606 performed in-depth functional and gene interaction analyses on the SM4/SM6 modules. The
607 module SM4 network included IGF1R and IGF2R among the displayed genes (Fig. 9A). Pathway
608 analysis revealed that SM4 genes were significantly over-represented in terms related to focal
609 adhesion, adherens junction, and the Rap1 signaling pathway (Fig. 9B; $p<0.05$). These pathways
610 are fundamentally involved in regulating cell-cell and cell-matrix interactions, cytoskeletal
611 dynamics, and cell migration. The up-regulation of SM4 therefore suggests an active
612 reorganization of the testicular stroma and basement membrane architecture in response to obesity.
613 In contrast, module SM6 presented a distinct signature centered on growth factor signaling and
614 metabolic regulation (Fig. 9A). It was notably enriched for multiple components of the insulin-like
615 growth factor (IGF) axis, including the ligand IGF1 and the high-affinity IGF-binding protein
616 IGFBP5 and the IGFBP-related protein IGFBP7 (Fig. 9A). Functional enrichment analysis linked
617 SM6 genes to the PI3K-Akt signaling pathway and focal adhesion, which are primary downstream
618 effectors of IGF receptor activation and are pivotal for promoting cell survival, proliferation, and
619 motility (Fig. 9B; $p<0.05$). In the gene-ranking analysis, IGF2R and IGF1R ranked 37th and 43rd
620 among 451 SM4 genes, respectively. Within SM6, IGFBP7 ranked 7th and IGFBP5 ranked 21st
621 among 247 genes, ahead of IGF1 (45th) and IGF2 (104th), supporting their prioritization as
622 candidate genes for further investigation (Fig. 9C).

623 A detailed examination of IGF family gene expression across the entire datasets solidified their
624 central role. Weighted correlation analysis showed a specific partitioning of IGF pathway
625 components between the two modules. The receptors IGF1R and IGF2R exhibited stronger

associations with SM4, whereas the ligands (IGF1, IGF2) and a subset of binding proteins (IGFBP5, IGFBP7 etc.) formed the core of SM6 (Fig. 9D). This suggests a potential paracrine or autocrine signaling loop where ligands from one cellular source (enriched in SM6) act on receptors present on adjacent cells (enriched in SM4). IGFBP5 and IGFBP7 showed more prominent expression than IGFBP3, suggesting distinct regulation of IGF bioavailability; however, IGFBP5 is a high-affinity IGF-binding protein, whereas IGFBP7 has substantially lower IGF-binding affinity [42, 43]. Cellular deconvolution analysis further contextualized this dysregulation, demonstrating that the expression of IGF1, IGFBP5, and IGFBP7 was most strongly correlated with macrophages, endothelial cells, myoid cells, and spermatogonia—precisely the cell populations whose proportions and spatial distributions were most altered in obesity (Fig. 9E). Supplementary Fig. S11 shows most of IGF family genes have higher spatial expression levels in obese individuals. We sought to validate these transcriptomic findings at the protein level and confirm their spatial context using multiplex immunofluorescence (Fig. 9F). Co-staining for the macrophage marker CD80 together with IGF1 and IGFBP7 in testicular sections provided compelling histological evidence. In testes from obese monkeys, we observed a marked intensification and a distinct spatial coalescence of IGF1 and IGFBP7 signals, which prominently co-localized with CD80+ macrophages. This was particularly evident in the interstitial space and the peritubular region immediately adjacent to the seminiferous tubule basement membrane (Fig. 9F, top panel). An analogous pattern was confirmed for IGF1 and IGFBP5 (Fig. 9F, bottom panel). In stark contrast, testicular sections from normal-weight animals displayed a more diffuse, lower-level expression of these proteins with less pronounced co-localization with macrophages. These images provide direct visual confirmation that obesity reshapes the testicular microenvironment into one where activated macrophages are strategically positioned and associated with a locally elevated IGF signaling milieu.

650 To elucidate the downstream transcriptional control mechanisms of the dysregulated IGF signaling
651 pathways, we constructed an analytical framework integrating transcriptional regulatory network
652 data with Topological Overlap Matrix (TOM) analysis. This approach enabled the identification of
653 key transcription factors (TFs) that may orchestrate the functional interactions between IGF family
654 genes and other non-IGF family genes within shared co-expression modules (Fig. 10A). TOM
655 analysis revealed strong topological correlations (wTO: weighted topological overlap; wTO>0.01,
656 $p<0.05$) between IGF family genes and other module members in SM4 and SM6, indicating their
657 close functional interconnectivity (Supplementary Fig. S12A, B). Pathway enrichment analysis
658 showed that these non-IGF family genes are involved in biological processes such as cell adhesion
659 and proliferation, aligning with the functional profile of IGF-related genes (Supplementary Fig.
660 S12A, B; $p<0.05$). Further network visualization identified specific TFs, including NFIA and
661 RORA (RAR-Related Orphan Receptor A), which appear to regulate non-IGF family genes within
662 SM4 and exhibit positive expression correlations with IGF1R and IGF2R (Fig. 10B, C;
663 wTO>0.01, $p<0.05$). Given that neither NFIA nor RORA acts as an upstream regulator of IGF1R
664 or IGF2R (Supplementary Fig. S12D; $p>0.05$), these findings suggest that IGF1R and IGF2R may
665 modulate the expression of non-IGF genes in SM4 through interactions with these TFs. Similarly,
666 we found that TFs such as EBF1 (Early B-Cell Factor 1) , NR2F2 (Nuclear Receptor Subfamily 2
667 Group F Member 2), NFIA, NFIB (Nuclear Factor I B) and RORA may serve as core mediators of
668 the interactions between IGF genes (IGF1, IGF2, IGFBP4, IGFBP5, IGFBP6 and IGFBP7) and
669 non-IGF family genes within the SM6 module (Supplementary Fig. S12D; Fig. 10B, C;
670 wTO>0.01, $p<0.05$). Following the same analytical approach, we further observed that IGF
671 signaling activation was linked to hormone receptors—including NR3C1, INSR, AR, FSHR, and
672 THRB—potentially through their regulatory effects on the expression of upstream transcription
673 factors of the IGF genes, such as EBF1, TCF4 (Transcription Factor 4), NFIA, NFIB
674 (Supplementary Fig. S12C-E; wTO>0.01, $p<0.05$). Differential regulon analysis identified these

key transcription factors (e.g., EBF1, NR2F2, NFIB) that up-regulate positive targets and down-regulate negative targets within SM4/SM6 in obese testes ($p<0.05$)—a pattern inverted in normal testes (Fig. 10D). They constructed the mutual positive regulation between SM4 and SM6, negative regulation of SM4/SM6 by SM2, SM8, and SM9 (Fig. 10E, F; $p<0.05$).

To investigate whether underlying genetic alterations could be a contributing factor to the observed transcriptional upregulation, we further performed copy number variation (CNV) analysis based on our single-cell (Supplementary Fig. S13) and spatial transcriptomic data (Supplementary Fig. S14). The inferred spatial CNV profiles revealed distinct expression-derived CNV patterns in obese testes compared to normal (Supplementary Fig. S14A). A comparative quantification showed a significant increase in the total CNV burden within specific cell populations from obese samples, most notably in macrophages, endothelial cells, myoid cells, and spermatogonia (Supplementary Fig. S14B; $p<0.05$). Crucially, when we focused specifically on the IGF family genes central to our hypothesis, we found that IGF1R and IGF2R ($p<0.05$)—the core receptors in SM4; IGF1 and IGFBP5 ($p<0.05$)—the core ligand and binding protein components in SM6—exhibited significantly elevated CNV scores in the obese group (Supplementary Fig. S14C). At a single-cell resolution, CNV scores for these genes were notably higher in macrophages, endothelial cells, myoid cells, and spermatogonia isolated from obese testes (Supplementary Fig. S14D; $p<0.05$). These expression-derived CNV scores do not establish somatic genomic alterations or focal amplifications without independent DNA-level validation. The CNV analysis from single-cell sequencing demonstrated similar patterns to the spatial transcriptomic CNV results, revealing increased inferred CNV scores in specific IGF genes within obese testicular tissues (Supplementary Fig. S13).

Discussion

The mechanisms underlying the impact of obesity on male reproductive function are highly complex and intertwined with genetic, endocrine, metabolic, and immunological factors [14, 15]. Consequently, researchers have yet to fully elucidate this pathological process [16]. Nevertheless, it is well established that obesity compromises the blood-testis barrier (BTB), which subsequently impairs spermatogenesis [14]. Current hypotheses regarding obesity-induced BTB disruption fall primarily into two categories: 1) obesity triggers the pathological atrophy of Sertoli cells and the aberrant secretion of tight junction-associated proteins, leading to structural alterations and the collapse of the BTB [17-20]; and 2) obesity provokes non-infectious testicular inflammation and oxidative stress, which disrupts the normal structure of the BTB and accelerates spermatogenic cell apoptosis [21-26]. Similar with the latter hypothesis, the results of this study demonstrate that obesity induces drastic alterations in the testicular microenvironment. These changes involve the aberrant polarization of testicular resident macrophages and their redistribution toward the seminiferous tubule boundary, increased inflammatory transcriptional signatures alongside enhanced inferred pro-inflammatory cell communication signaling, thickening of the seminiferous tubule basement membrane, reduced developmental potential and increased cell death-related gene set scores in spermatogenic cells, and dysregulated steroid metabolism within Leydig cells. This microenvironmental derangement in obese testes is a multicellular process driven by macrophages, myoid cells, endothelial cells, spermatogonia, round spermatids, and Leydig cells, among which macrophages appear to act as the trigger for this cascade. Previous researches suggested that obesity-induced chronic testicular inflammation stems from systemic imbalances in the peripheral immune system, wherein circulating pro-inflammatory factors and immune cell infiltration alter the BTB structure, leading to spermatogenic cell destruction [14, 21-25]. In contrast, this study identifies local IGF-associated transcriptional changes in obese testes despite no significant differences in the measured circulating immune factors; these observations do not exclude a

contribution from systemic inflammation. This anomalous gene expression profile prompts a fundamental reconsideration of the role of the IGF family genes during spermatogenesis.

The insulin-like growth factor (IGF) gene family primarily comprises IGF ligand genes (IGF1, IGF2), IGF receptor genes (IGF1R, IGF2R), and IGF-binding proteins (e.g., IGFBP3, IGFBP5, IGFBP7), with the IGF ligand genes exerting a central role [27]. These ligand genes are predominantly expressed and secreted by Sertoli cells, Leydig cells, and spermatogonia, among which Sertoli cells serve as the primary source of IGF factors [28]. Previous literature has consistently established that IGF signaling is a critical factor for maintaining the stemness and survival of spermatogonia, promoting meiosis and spermatogenesis, regulating tight junction protein secretion to maintain the structural integrity of BTB, and optimizing testosterone synthesis in Leydig cells [28-34]. Consequently, altered IGF-related measures have been investigated in relation to semen quality and male infertility [30, 35, 36]. Theoretically, signaling transduction between IGF ligands and their receptors occurs internally among Sertoli cells, germ cells, and Leydig cells. In contrast, this study demonstrates that under obese conditions, intensive IGF-mediated cell-cell communication networks emerge aberrantly among macrophages, peritubular myoid cells, endothelial cells, spermatogonia and Leydig cells. Since the downstream PI3K/AKT pathway triggered by IGF1 is closely tied to cellular proliferation [37], this rewired communication pattern may directly fuel the aberrant expansion of myoid and endothelial cells, culminating in the observed hyperplasia of the seminiferous tubule basement membrane. Concurrently, this altered IGF signaling cascade precipitates comprehensive shifts in downstream gene expression. Consequently, these co-expressed gene modules promote resident macrophage polarization, disrupt steroid metabolism within Leydig cells, compromise SSC stemness, and ultimately impair spermatogenesis. Although existing literature has not explicitly documented a high baseline expression of IGF1 protein in testicular resident macrophages, evidence from other organs, particularly in tumor tissues, has confirmed that immune cells, including macrophages,

747 can aberrantly upregulate IGF1 expression to sustain tumor cell proliferation and stimulate
748 peripheral tissue and vascular hyperplasia [38-41]. Collectively, these insights suggest that
749 testicular IGF proteins do not universally exert beneficial effects on spermatogenesis; instead, they
750 may precipitate detrimental pathological outcomes depending on the specific microenvironmental
751 context.
752 The functional outcomes of IGF signaling are likely dictated by the types of its binding proteins
753 (IGFBPs). The biological activity of the IGF1 protein is primarily regulated by IGFBP3, which
754 efficiently binds to IGF1, prolongs its half-life, and simultaneously reduces free IGF1 levels to
755 prevent its excessive tissue stimulation [42-44]. Intriguingly, we found that cynomolgus monkey
756 testicular cells exhibit negligible expression of IGFBP3; instead, IGF1 is co-expressed with
757 IGFBP5 and IGFBP7. IGFBP5 belongs to the high-affinity IGF-binding proteins, whereas
758 IGFBP7 is an IGFBP-related protein with substantially lower affinity for IGFs [42, 43]. Co-
759 expression and co-localization do not establish direct binding or the concentration of free IGF1, so
760 the effects on IGF bioavailability and BTB integrity remain to be established. Apart from their
761 canonical IGF-1-binding capacity, IGFBP-5 and IGFBP-7 possess intrinsic, IGF-independent
762 biological activities that are strictly contingent upon the pathological context. Growing evidence
763 positions IGFBP5 and IGFBP7 as critical mediators in the pathogenesis of diabetic complications
764 [45-48]. Notably, the inhibition of IGFBP7 via 5-methyltetrahydrofolate (5-MTHF) delivery in
765 diabetic mice blunts downstream STAT3 signaling, thereby arresting diabetic nephropathy
766 progression, reducing lipid deposition, and reversing renal tubular impairment [46]. Obesity and
767 diabetes share highly conserved biological mechanisms characterized by endocrine dysfunction,
768 metabolic abnormalities, and insulin resistance. Consequently, the upregulation of IGFBP5 and
769 IGFBP7 in the testes under obese conditions may functionally parallel their roles in diabetic
770 nephropathy by driving inflammation and tissue injury. We further demonstrate that testicular
771 IGF1, IGFBP5, and IGFBP7 orchestrate a co-expression network with key male reproductive

genes and transcription factors, including EBF1 and NR2F2 [49]. Expression of this gene module is associated with pro-inflammatory macrophage polarization, altered steroidogenic transcription and reduced BTB-related gene expression. Notably, the dysregulation of IGF1, IGFBP5, and IGFBP7 correlates closely with insulin and glucocorticoid receptors, supporting their investigation as potential mediators of obesity-associated testicular dysfunction.

Conclusions

Our integrated single-cell and spatial transcriptomic analyses reveal coordinated remodeling of the testicular microenvironment in obesity, characterized by peritubular macrophage accumulation, enhanced inflammatory signaling, altered somatic-cell niches, and impaired spermatogenic transcriptional programs. These changes are accompanied by reduced expression of blood–testis barrier-associated genes and proteins, suppressed steroidogenic programs, and stage-specific disruption of germ-cell development. Within this remodeled niche, the compartmentalized upregulation of IGF1, IGFBP5, and IGFBP7, together with the spatial organization of IGF receptor-expressing cells, identifies a locally dysregulated IGF-associated signaling network. These components may emerge as candidate moleculars link between inflammatory niche remodeling and obesity-associated testicular dysfunction. Collectively, our findings provide a spatially resolved framework for understanding obesity-related spermatogenic impairment and establish a molecular basis for future research into the cellular interactions and signaling pathways governing testicular homeostasis and male reproductive health.

List of abbreviations

AF, anti-inflammatory factors; BTB, blood-testis barrier; CNV, copy number variation; DEG, differentially expressed gene; hdWGCNA, high-dimensional weighted gene co-expression network analysis; IGF, insulin-like growth factor; PF, pro-inflammatory factors; RCTD, robust cell type decomposition; scRNA-seq, single-cell RNA sequencing; SM, spatial module; ST,

spatial transcriptomics; TF, transcription factor; TOM, topological overlap matrix; UMAP, uniform manifold approximation and projection.

Declarations

Ethics approval and consent to participate

All animal procedures were approved by the Institutional Animal Care and Use Committee of the Laboratory Animal Center, Nanhu Laboratory (IACUC-DWZX-2024-051; 4 January 2025) and were performed in accordance with the approved protocol and relevant institutional guidelines and regulations.

Consent for publication

Not applicable.

Availability of data and materials

All sequencing data generated in this study have been deposited in the Genome Sequence Archive (GSA; https://ngdc.cncb.ac.cn/gsa/) under accession number CRA034245. All other data supporting the findings of this study are available from the corresponding authors upon reasonable request. No previously unreported custom algorithm was developed for this study; analyses were performed using the software and parameters described in the Materials and Methods.

Competing interests

The authors declare no competing financial or non-financial interests.

Funding

This work was supported by the Nanhu Laboratory self-initiated research project (NSS2023A00001-1).

Authors' contributions

K.Y., S.D., and Y.Q. conceived the study. Y.L., D.W., Y.Y., and S.D. collected cynomolgus monkey testis samples. T.Z. optimized the experimental conditions and established the experimental methods. D.W. and T.Z. constructed the spatial transcriptomic libraries. Y.Z. performed the bioinformatics analyses. Y.L. performed the staining experiments. Y.L., Y.Z., and K.C. interpreted the data. Y.L., Y.Z., and D.W. wrote the manuscript with input from all authors. J.L., R.Z., S.S., J.H., and Y.K. contributed to manuscript revision. All authors reviewed and approved the final manuscript. Y.L., D.W., Y.Y., and T.Z. contributed equally to this work.

Acknowledgements

Not applicable.

References

1. Collaborators GBDAB. Global, regional, and national prevalence of adult overweight and obesity, 1990-2021, with forecasts to 2050: a forecasting study for the Global Burden of Disease Study 2021. Lancet. 2025;405(10481):813-38.

2. Bray GA. Evaluation of obesity. Who are the obese? Postgrad Med. 2003;114(6):19-27, 38.

3. Kivimaki M, Strandberg T, Pentti J, Nyberg ST, Frank P, Jokela M, et al. Body-mass index and risk of obesity-related complex multimorbidity: an observational multicohort study. Lancet Diabetes Endocrinol. 2022;10(4):253-63.

4. Finkelstein JS, Yu EW, Burnett-Bowie SA. Gonadal steroids and body composition, strength, and sexual function in men. N Engl J Med. 2013;369(25):2457.

5. Miyaso H, Ogawa Y, Itoh M. Microenvironment for spermatogenesis and sperm maturation. Histochem Cell Biol. 2022;157(3):273-85.

6. Oatley JM, Brinster RL. The germline stem cell niche unit in mammalian testes. Physiol Rev. 2012;92(2):577-95.

7. Andersen JM, Herning H, Aschim EL, Hjelmesaeth J, Mala T, Hanevik HI, et al. Body Mass Index Is Associated with Impaired Semen Characteristics and Reduced Levels of Anti-Mullerian Hormone across a Wide Weight Range. PLoS One. 2015;10(6):e0130210.

8. Nguyen RH, Wilcox AJ, Skjaerven R, Baird DD. Men's body mass index and infertility. Hum Reprod. 2007;22(9):2488-93.

9. Nie X, Munyoki SK, Sukhwani M, Schmid N, Missel A, Emery BR, et al. Single-cell analysis of human testis aging and correlation with elevated body mass index. Dev Cell. 2022;57(9):1160-76 e5.

10. Cui L, Nie X, Guo Y, Ren P, Guo Y, Wang X, et al. Single-cell transcriptomic atlas of the human testis across the reproductive lifespan. Nat Aging. 2025;5(4):658-74.

11. Larsson L, Frisen J, Lundeberg J. Spatially resolved transcriptomics adds a new dimension to genomics. Nat Methods. 2021;18(1):15-8.

12. Fayomi AP, Orwig KE. Spermatogonial stem cells and spermatogenesis in mice, monkeys and men. Stem Cell Res. 2018;29:207-14.

13. Huang D, Zuo Y, Zhang C, Sun G, Jing Y, Lei J, et al. A single-nucleus transcriptomic atlas of primate testicular aging reveals exhaustion of the spermatogonial stem cell reservoir and loss of Sertoli cell homeostasis. Protein & Cell. 2022.

14. Cannarella R, Crafa A, Curto R, Condorelli RA, La Vignera S, Calogero AE. Obesity and male fertility disorders. Molecular aspects of medicine. 2024;97:101273.

15. Li X, Lin J, Wu M, Han F, Chen S, Ke H, et al. Ergothioneine rescues obesity-induced testicular dysfunction via dual restoration of steroidogenesis and mitochondrial redox homeostasis. Redox Biology. 2026:104090.

16. Uddandrao V, Brahma Naidu P, Chandrasekaran P, Saravanan G. Pathophysiology of obesity-related infertility and its prevention and treatment by potential phytotherapeutics. International journal of obesity. 2024;48(2):147-65.

17. Pan M, Zhao H, Xu F, Li J, Liu Z, Li L, et al. Zhuling Yanzong formula ameliorates obesity-induced oligoasthenozoospermia via regulating HSL/StAR and HSL/TIMP-1. Journal of Ethnopharmacology. 2025:120319.

18. Zhang G, Wang Z, He M, Kong L, Yushanjiang S, Jin L, et al. A High-Fat Diet Damages the Blood-Testis Barrier Through the PCSK9-LOX1 Positive Feedback Loop in Sertoli Cells. Reproductive Sciences. 2025:1-12.

19. Mu Y, Yin T-l, Zhang Y, Yang J, Wu Y-t. Diet-induced obesity impairs spermatogenesis: the critical role of NLRP3 in Sertoli cells. Inflammation and Regeneration. 2022;42(1):24.

20. Cannarella R, Curto R, Condorelli RA, Lundy SD, La Vignera S, Calogero AE. Molecular insights into Sertoli cell function: how do metabolic disorders in childhood and adolescence affect spermatogonial fate? Nature communications. 2024;15(1):5582.

21. Leisegang K, Sengupta P, Agarwal A, Henkel R. Obesity and male infertility: Mechanisms and management. Andrologia. 2021;53(1):e13617.

22. Suleiman JB, Nna VU, Zakaria Z, Othman ZA, Bakar ABA, Mohamed M. Obesity-induced testicular oxidative stress, inflammation and apoptosis: Protective and therapeutic effects of orlistat. Reproductive Toxicology. 2020;95:113-22.

23. Fan W, Xu Y, Liu Y, Zhang Z, Lu L, Ding Z. Obesity or overweight, a chronic inflammatory status in male reproductive system, leads to mice and human subfertility. Frontiers in physiology. 2018;8:1117.

24. Ma Y, Yu X, Liu YF, Song B, Sun Z, Zhao S. Immunoregulation and male reproductive function: Impacts and mechanistic insights into inflammation. Andrology. 2025;13(6):1302-21.

25. Leisegang K, Henkel R, Agarwal A. Obesity and metabolic syndrome associated with systemic inflammation and the impact on the male reproductive system. American journal of reproductive immunology. 2019;82(5):e13178.

890 26. Ye J, Luo D, Xu X, Sun M, Su X, Tian Z, et al. Metformin improves fertility in obese males
891 by alleviating oxidative stress-induced blood-testis barrier damage. Oxidative medicine and
892 cellular longevity. 2019;2019(1):9151067.
893 27. LeRoith D, Holly JM, Forbes BE. Insulin-like growth factors: Ligands, binding proteins, and
894 receptors. Molecular metabolism. 2021;52:101245.
895 28. Griffeth RJ, Bianda V, Nef S. The emerging role of insulin-like growth factors in testis
896 development and function. Basic and clinical andrology. 2014;24(1):12.
897 29. Spiteri-Grech J, Nieschlag E. The role of growth hormone and insulin-like growth factor I in
898 the regulation of male reproductive function. Hormone research. 1992;38:22-.
899 30. Fu L, Yuen KC, Tint AN, Hoffman AR, Bongso AT, Lee KO. Association of decreased sperm
900 motility and increased seminal plasma IGF-I, IGF-II, IGFBP-2, and PSA levels in infertile men.
901 Endocrine. 2021;74(3):698-706.
902 31. Liu G, Liu D, Zhu M, Zhang M, Li C, Xu X, et al. Insulin-like growth factor-1 promotes the
903 testicular sperm production by improving germ cell survival and proliferation in high-fat diet-
904 treated male mice. Andrology. 2025;13(2):342-58.
905 32. Wang G, Hardy MP. Development of leydig cells in the insulin-like growth factor-I (igf-I)
906 knockout mouse: effects of igf-I replacement and gonadotropic stimulation. Biology of
907 Reproduction. 2004;70(3):632-9.
908 33. Neirijnck Y, Calvel P, Kilcoyne KR, Kühne F, Stévant I, Griffeth RJ, et al. Insulin and IGF1
909 receptors are essential for the development and steroidogenic function of adult Leydig cells. The
910 FASEB Journal. 2018;32(6):3321–35.
911 34. Tenuta M, Carlomagno F, Cangiano B, Kanakis G, Pozza C, Sbardella E, et al. Somatotropic-
912 Testicular Axis: A crosstalk between GH/IGF-I and gonadal hormones during development,
913 transition, and adult age. Andrology. 2021;9(1):168-84.

914 35. Cannarella R, La Vignera S, Condorelli RA, Calogero AE. The IGF1/FSH Ratio Correlates
915 with Sperm Count and Testicular Volume. Endocrines. 2022;3(4):624-32.
916 36. Vashisht A, Gahlay GK. Understanding seminal plasma in male infertility: emerging markers
917 and their implications. Andrology. 2024;12(5):1058-77.
918 37. Deng C-Y, Lv M, Luo B-H, Zhao S-Z, Mo Z-C, Xie Y-J. The role of the PI3K/AKT/mTOR
919 signalling pathway in male reproduction. Current molecular medicine. 2021;21(7):539-48.
920 38. Pang Y-C, Wang C, Qiu J-F, Chen H-X, Deng K, Feng Z, et al. Targeting tumor-associated
921 macrophage-induced IGF1/PI3K/Zic1 axis triggers SHH medulloblastoma regression and
922 chemosensitization. Neuro-Oncology. 2026;28(6):1556-70.
923 39. Sanchez-Lopez E, Flashner-Abramson E, Shalapour S, Zhong Z, Taniguchi K, Levitzki A, et
924 al. Targeting colorectal cancer via its microenvironment by inhibiting IGF-1 receptor-insulin
925 receptor substrate and STAT3 signaling. Oncogene. 2016;35(20):2634-44.
926 40. Harvey AE, Lashinger LM, Otto G, Nunez NP, Hursting SD. Decreased systemic IGF-1 in
927 response to calorie restriction modulates murine tumor cell growth, nuclear factor-κB activation,
928 and inflammation -related gene expression. Molecular carcinogenesis. 2013;52(12):997-1006.
929 41. Spadaro O, Camell CD, Bosurgi L, Nguyen KY, Youm Y-H, Rothlin CV, et al. IGF1 shapes
930 macrophage activation in response to immunometabolic challenge. Cell reports. 2017;19(2):225-
931 34.
932 42. Daza DO, Sundström G, Bergqvist CA, Duan C, Larhammar D. Evolution of the insulin-like
933 growth factor binding protein (IGFBP) family. Endocrinology. 2011;152(6):2278-89.
934 43. Hwa V, Oh Y, Rosenfeld RG. The insulin-like growth factor-binding protein (IGFBP)
935 superfamily. Endocrine reviews. 1999;20(6):761-87.
936 44. Ranke MB. Insulin-like growth factor binding-protein-3 (IGFBP–3). Best practice & research
937 Clinical endocrinology & metabolism. 2015;29(5):701-11.

938 45. Yu J-t, Xie S-s, Shen X-y, Li Z, Hu X-w, Zhang Y, et al. Renal tubular epithelial IGFBP7
939 interacts with PKM2 to drive renal lipid accumulation and fibrosis. Molecular Therapy.
940 2025;33(8):3757-77.
941 46. Yu J-t, Hu X-w, Wang J-n, Yang Q, Li X-y, Shan R-r, et al. Renal insulin-like growth factor
942 binding-protein 7 is a critical promoter of progressive diabetic kidney disease. Nature
943 Communications. 2025.
944 47. Hu X, Chen W, Yang M, Li M, Li X, Ouyang S. IGFBP5 promotes EndoMT and renal fibrosis
945 through H3K18 lactylation in diabetic nephropathy: X. Hu et al. Cellular and Molecular Life
946 Sciences. 2025;82(1):215.
947 48. Song C, Wang S, Fu Z, Chi K, Geng X, Liu C, et al. IGFBP5 promotes diabetic kidney disease
948 progression by enhancing PFKFB3-mediated endothelial glycolysis. Cell death & disease.
949 2022;13(4):340.
950 49. Estermann MA, Grimm SA, Kitakule AS, Rodriguez KF, Brown PR, McClelland K, et al.
951 NR2F2 regulation of interstitial cell fate in the embryonic mouse testis and its impact on
952 differences of sex development. Nature Communications. 2025;16(1):3987.

953 **Figure legends**

954 Fig. 1. Single-cell transcriptomic atlas and spatial cell-type mapping of cynomolgus monkey
955 testes. (A) The workflow of multi-omics analysis of testes. (B) The UMAP plot showing the
956 annotated cell-types of monkey testes. Each dot represents a single testicular cell and each color
957 represents a cell-type. (C) Dot plot of marker gene expression across the annotated cell types. Dot
958 size represents the percentage of expressing cells, and color represents mean expression scaled as
959 a gene-wise z-score. (D) Characterization of spatial transcriptomics data using single-cell cell-type
960 deconvolution. (E) Spatial mapping of the predominant cell type. (F) Spatial distributions of
961 spermatogenic and non-spermatogenic cell populations. SPGs, spermatogonia; SPCs,

962 spermatocytes; Round, round spermatids; Elongating, elongating spermatids; Elongated, elongated
963 spermatids; Sertoli, Sertoli cells; Macrophage, macrophages; Myoid, myoid cells; LCs, Leydig
964 cells; ILCs, immature Leydig cells; Endothelial, endothelial cells.
965 Fig. 2. Comparison of cellular composition between groups with spatial transcriptomics. (A) The
966 proportion of cell-types within testis. (B) Box plots with statistical results showing changes in the
967 proportion of cell-types ($p < 0.05$). (C) The ratio of observed over expected numbers (Ro/e) of
968 cell-types within the testes from normal and obese cynomolgus monkeys. (D) Hematoxylin and
969 eosin (HE) stained sections of testicular tissues. (E) Representative examples from both normal
970 and obesity samples showing cell-(top) and transcript/molecular-based (bottom) niches. For cell
971 niches, each point is a cell centroid. (F) Preference differences (normal vs. obesity) of cell-(left)
972 and transcript-based (right) niches. (G) Cell assignment to cell-(top) and transcript-based (bottom)
973 niches. SPGs, spermatogonia; SPCs, spermatocytes; Round, round spermatids; Elongating,
974 elongating spermatids; Elongated, elongated spermatids; Sertoli, Sertoli cells; Macrophage,
975 macrophages; Myoid, myoid cells; LCs, Leydig cells; ILCs, immature Leydig cells; Endothelial,
976 endothelial cells.
977 Fig. 3. Results of spatial co-localization analysis. (A) Bar plots showing the changes of the
978 minimum distance between macrophage and other cell-types in the normal and obesity testes. (B)
979 The standardized importance values (median) of the intrinsic (left) and juxta (right) views between
980 macrophage and other cell-types. The higher importance values represent higher dependencies
981 between different cell-types within spots (intrinsic view) or immediate neighbour spots (juxta
982 view). (C) Comparative analysis of nearest neighbor cell proportions between normal and obese
983 testes from cynomolgus monkeys by leveraging spatial transcriptomic sequencing (ST-seq) data.
984 (D) Spatial feature plots showing the macrophage and seminiferous tubule basement membrane
985 (STBM). SPGs, spermatogonia; SPCs, spermatocytes; Round, round spermatids; Elongating,
986 elongating spermatids; Elongated, elongated spermatids; Sertoli, Sertoli cells; Macrophage,

macrophages; Myoid, myoid cells; LCs, Leydig cells; ILCs, immature Leydig cells; Endothelial, endothelial cells.

Fig. 4. Gene set score analysis of macrophage polarization. (A) Spatial feature plots showing the distribution of macrophage sub types (M0 Macrophage, M1-Macrophage M2+ Macrophage, M1+ Macrophage M2-Macrophage, M1+ Macrophage M2+ Macrophage). (B) Spatial feature plots showing the distribution of inflammation and anti-inflammation regions (PF+ AF+ Region, PF+ AF-Region, PF-AF+ Region). (C) Spatial feature plots showing the distribution of PF+ AF+ Region (left), and the counts of related cell-types (right). (D) Spatial feature plots showing the distribution of PF+ AF-Region (left), and the counts of related cell-types (right). (E) Spatial feature plots showing the distribution of PF-AF+ Region (left), and the counts of related cell-types (right). SPGs, spermatogonia; SPCs, spermatocytes; Round, round spermatids; Elongating, elongating spermatids; Elongated, elongated spermatids; Sertoli, Sertoli cells; Macrophage, macrophages; Myoid, myoid cells; LCs, Leydig cells; ILCs, immature Leydig cells; Endothelial, endothelial cells.

Fig. 5. Results of cell-cell communication analysis based on ST-seq data. (A) Circle plots (by CellChat analysis) depicting the differential number of interactions (left) or interaction strength (right) in the cell-cell communication network between normal and obesity. Red or blue edges represent increased or decreased signaling in obesity compared with normal, respectively. (B) Analysis of the incoming or outgoing interaction strength of different cells in normal and obese groups. (C) Bar plots showing the relative information flow between normal and obese groups. (D) Heatmap showing the unique cell-cell communication signals in obese groups (marked with blue words) and normal groups (marked with red words). Color intensity represents the communication probability. SPGs, spermatogonia; SPCs, spermatocytes; Round, round spermatids; Elongating, elongating spermatids; Elongated, elongated spermatids; Sertoli, Sertoli

cells; Macrophage, macrophages; Myoid, myoid cells; LCs, Leydig cells; ILCs, immature Leydig cells; Endothelial, endothelial cells.

Fig. 6. Expression of blood-testis barrier (BTB) and steroid metabolism-related genes in testicular tissue. (A) Bar plots showing the BTB-(top) and steroid metabolism-(bottom) related gene expression in ST-seq data after SCT-transformation. (B) Spatial feature plots showing the expression levels of representative genes (CLDN11/claudin11 and GATA4) in BTB and (CYP17A1, CYP19A1) in steroid metabolism. (C) Immunofluorescence stained sections for CLDN11 (left) and immunohistochemistry stained sections for GATA4 (right). For proteins with relatively low expression levels, the immunofluorescence presents better results compared to immunohistochemistry.

Fig. 7. The pseudotime analysis of spermatogenesis based on scRNA-seq data. (A) The pseudotime analysis of germ cells along the spermatogenesis process in monkey testes (top), and the distribution of normal and obesity groups along the pseudotime trajectory (bottom). (B) Box plots showing the developmental potential score of different germ cell-types in normal and obese testicular tissue (top), and the heatmap of potency-associated scores across spermatogenic cell-types with varying differentiation potential (bottom). (C) The heatmap of expression levels and enriched pathways of DEGs along pseudotime trajectory. These DEGs were clustered into 5 groups. (D) Expression levels of the gene set in each cluster across different cell-types (left) and their spatial distribution (right). (E) Box plots showing the representative gene set scores for spermatogenesis, mitosis, meiosis, spermatid differentiation, cilium organization and sperm motility. SPGs, spermatogonia; SPCs, spermatocytes; Round, round spermatids; Elongating, elongating spermatids; Elongated, elongated spermatids; Sertoli, Sertoli cells; Macrophage, macrophages; Myoid, myoid cells; LCs, Leydig cells; ILCs, immature Leydig cells; Endothelial, endothelial cells.

Fig. 8. Functions and distributions of spatial co-expression gene modules identified by hdWGCNA. (A) The gene set expression levels of each module in normal and obesity samples. (B) Heatmap showing the Spearman correlation between different gene modules. (C) Heatmap showing the correlations between different gene modules and M1 Polarization, BTB Integrity, M2 Polarization, and Steroid Metabolism. (D) Matching diagram showing the correlation trends of BTB integrity with SM4 and SM6 gene sets in normal and obese testes. (E) The enriched cell-types of each module. (F) Spatial feature plots showing the distribution and expression levels of SM4 and SM6 genes in the testicular tissue from normal and obese monkeys. SPGs, spermatogonia; SPCs, spermatocytes; Round, round spermatids; Elongating, elongating spermatids; Elongated, elongated spermatids; Sertoli, Sertoli cells; Macrophage, macrophages; Myoid, myoid cells; LCs, Leydig cells; ILCs, immature Leydig cells; Endothelial, endothelial cells.

Fig. 9. The core genes of modules SM4 and SM6. (A) Gene co-expression networks of SM4 (top; IGF1R and IGF2R highlighted) and SM6 (bottom). (B) Bar plots showing enriched pathways of SM4 genes (top) and SM6 genes (bottom). (C) Gene rankings by mean residual rank correlation in SM4 (top, 451 genes) and SM6 (bottom, 247 genes), with selected IGF-related genes labeled. (D) Heatmap of IGF-related gene associations with co-expression modules. (E) Heatmap showing IGF-related gene expression across cell types. (F) Immunofluorescence stained sections for CD80-IGF1-IGFBP7 (top) and CD80-IGF1-IGFBP5 (bottom). SPGs, spermatogonia; SPCs, spermatocytes; Round, round spermatids; Elongating, elongating spermatids; Elongated, elongated spermatids; Sertoli, Sertoli cells; Macrophage, macrophages; Myoid, myoid cells; LCs, Leydig cells; ILCs, immature Leydig cells; Endothelial, endothelial cells.

Fig. 10. Inferred transcriptional regulatory relationships of IGF-related genes within SM4 and SM6. (A) The workflow of transcriptional regulatory network analysis for identifying transcription factors (TFs) mediating gene interactions. Condition 1: gene A influences the

expression of gene C through its interaction with transcription factor B; Condition 2: transcription factor B regulates the expression of both gene A and gene C; Condition 3: gene A influences the expression of gene C but is independent of its upstream regulator B. (B) Network plots depicting potential upstream TFs of non-IGF family genes in the modules of SM4 (left) and SM6 (right). (C) Heatmap plots showing the correlation of IGF family genes in the modules of SM4 (left) and SM6 (right) with the TFs presented in (B). (D) Scatter plot depicting the differential regulons between groups. An increased average Log2FC value for positive regulons signifies the up-regulation of TF-activated (positively regulated) genes in normal testes and their down-regulation in obese testes; likewise, an increased average Log2FC for negative regulons indicates the up-regulation of TF-repressed (negatively regulated) genes in normal testes and their down-regulation in obese testes. Upper-left quadrant TFs: their activated genes are up-regulated, while their repressed genes are down-regulated in obese testes. Lower-right quadrant TFs: their activated genes are up-regulated, while their repressed genes are down-regulated in normal testes. (E) Heatmap showing the positive regulatory scores and the numbers of positive TF-target gene regulatory connections across different SM gene sets. (F) Heatmap showing the negative regulatory scores and the numbers of negative TF-target gene regulatory connections across different SM gene sets.

Table 1. Differences in semen parameters between the normal and obese groups.

Semen Parameters	**Obesity**	**Normal**	**p-value**
Survival Rate (%)	31.48±5.41	93.39±2.35	<0.001
Motility (%)	22.77±5.31	82.05±3.99	<0.001
Concentration (10^6/mL)	2.03±0.26	6.66±0.83	0.006
VCL (μm/s)	46.03±3.55	160.63±7.69	<0.001
VSL (μm/s)	23.52±3.81	106.99±11.07	0.002
LIN (ratio)	0.23±0.03	0.57±0.03	0.001
STR (ratio)	0.39±0.04	0.77±0.02	<0.001

Semen Parameters	Obesity	Normal	p-value
VAP (μm/s)	1.49±0.17	5.95±0.41	<0.001
ALH (μm)	5.85±0.37	17.61±0.86	<0.001
WOB (ratio)	0.49±0.03	0.71±0.01	0.003

VCL, curvilinear velocity; VSL, straight line velocity; LIN, linearity; STR, straightness; VAP, average path velocity; ALH, amplitude of lateral head displacement; WOB, wobble. Data were expressed as mean ± standard error of the mean (SEM). One-way ANOVA was used for statistical analysis.

Table 2. Differences in blood hormones between the normal and obese groups.

Hormones	Obesity	Normal	p-value
FSH	0.95±0.21	1.05±0.58	0.916
LH	0.39±0.61	1.61±0.33	0.151
T	0.91±0.68	1.09±0.65	0.848
E2	1.75±0.62	0.25±0.45	0.044
COR	0.99±0.60	1.01±0.13	0.988
FERR	0.33±0.78	1.67±0.61	0.094
INS	1.46±0.16	0.54±0.19	0.309
Leptin	1.31±0.81	0.69±0.79	0.516
ADI	1.87±0.69	0.13±0.28	0.004

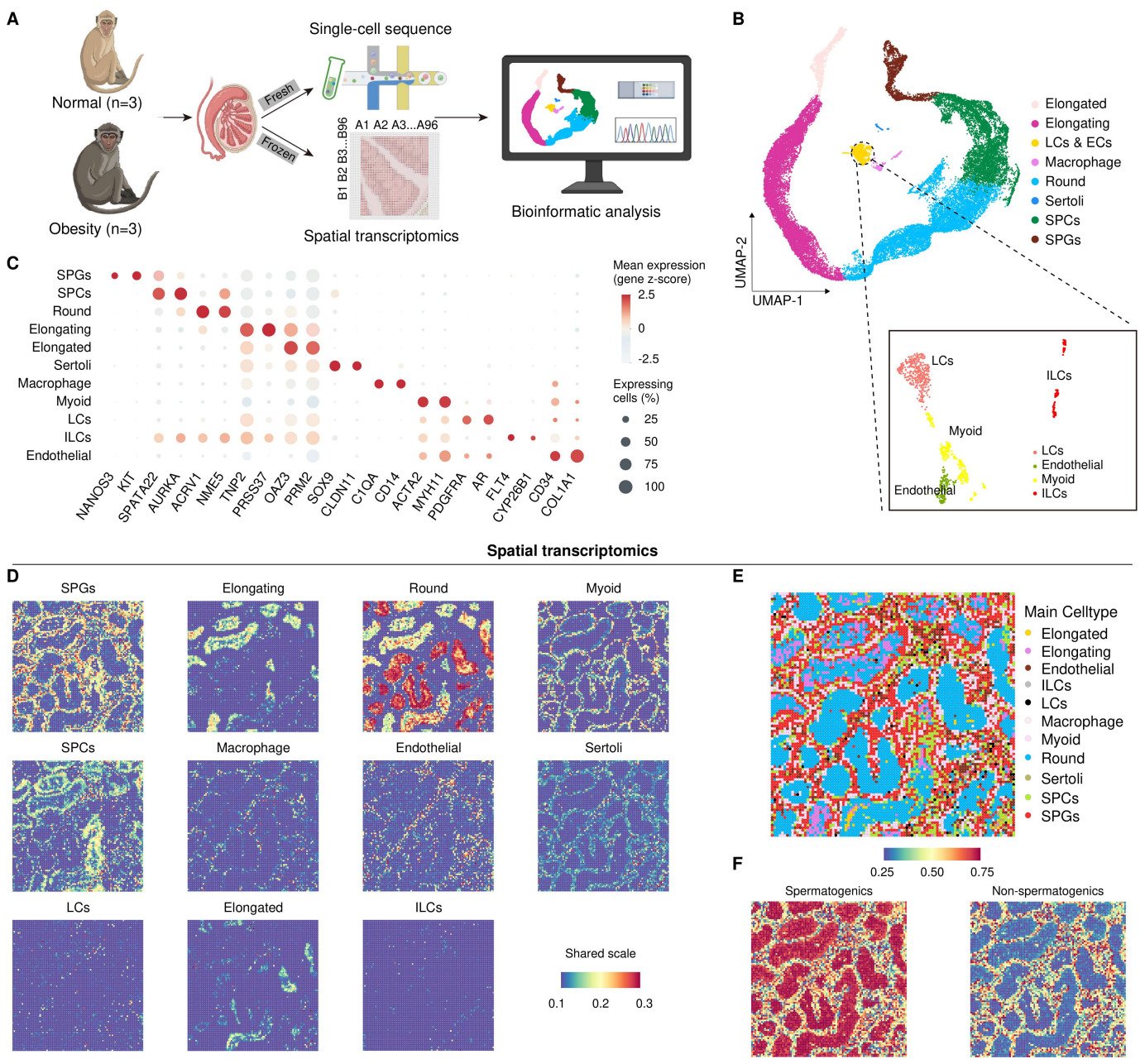
FSH, follicle-stimulating hormone; LH, luteinizing hormone; T, testosterone; E2, estradiol; COR, cortisol; FERR, ferritin; INS, insulin; ADI, adiponectin. Data were expressed as mean ± standard error of the mean (SEM). One-way ANOVA was used for statistical analysis.

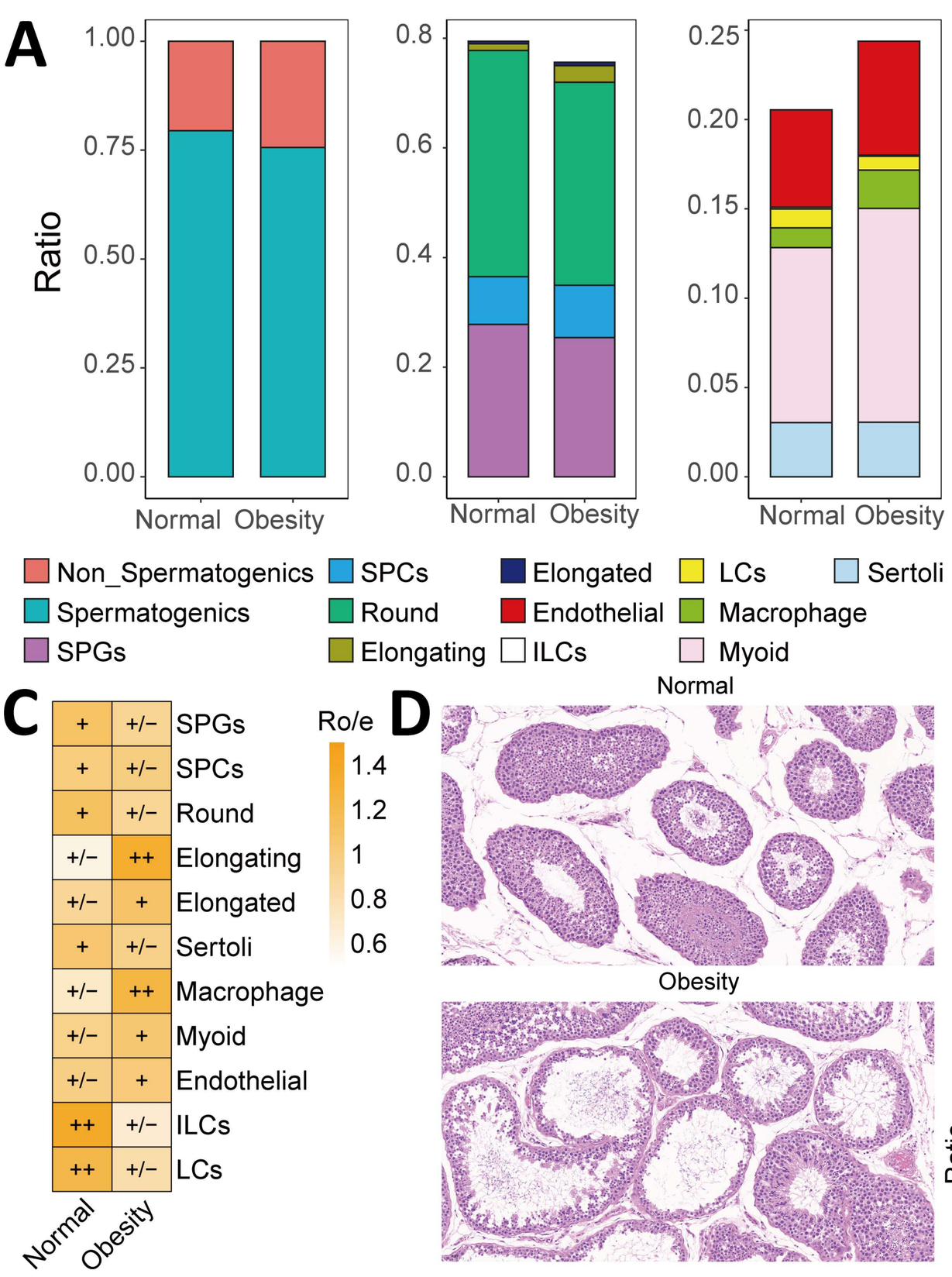
Table 3. Differences in immune factors between the normal and obese groups.

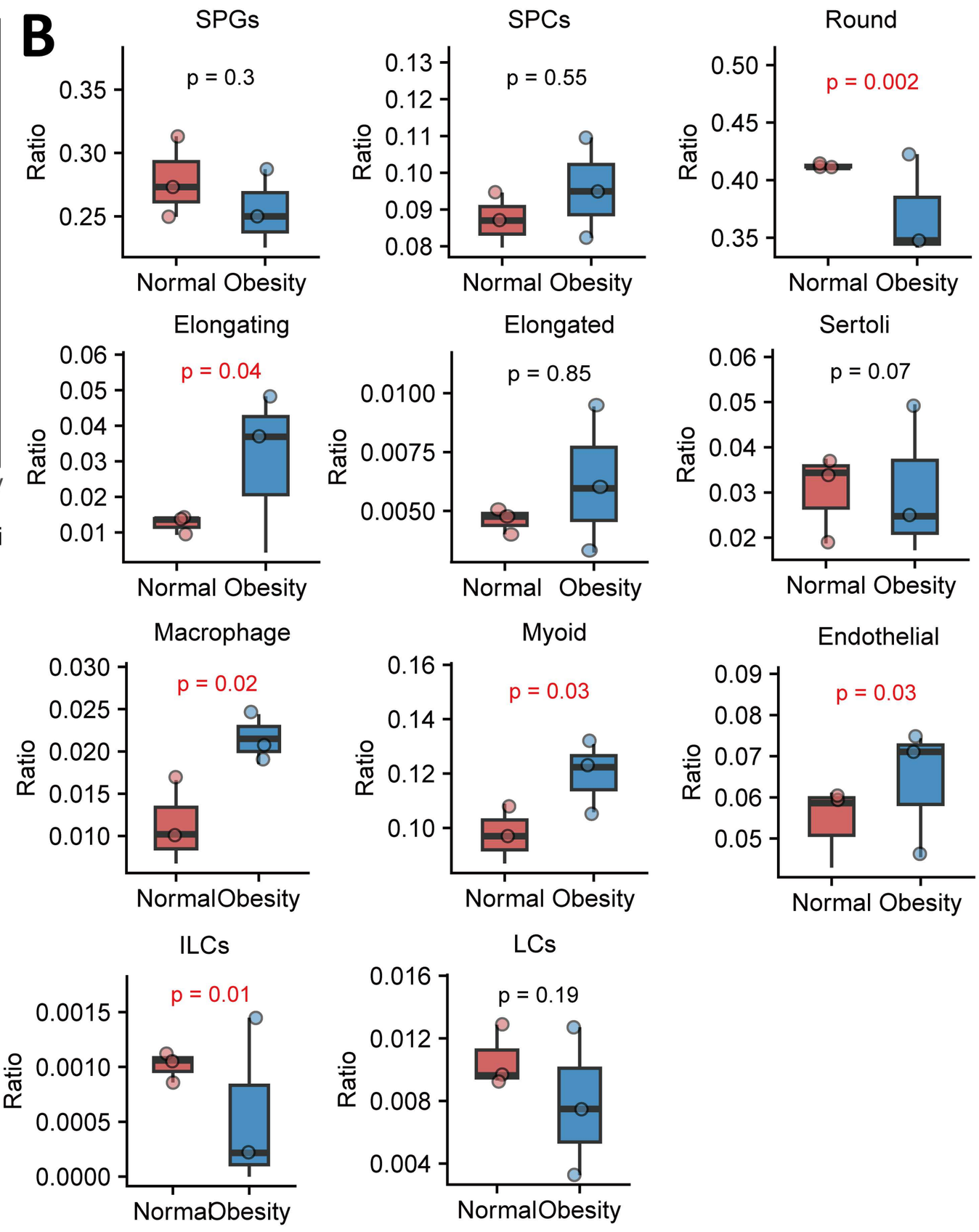
Immune Factors	Obesity	Normal	p-value
IFN-γ	1.61±0.61	0.39±0.45	0.144
IL-10	1.11±0.33	0.89±0.64	0.822

Immune Factors	Obesity	Normal	p-value
IL-4	1.24±0.62	0.76±0.55	0.618
IL-1β	1.26±0.75	0.74±0.62	0.592
TNF-α	0.67±0.87	1.33±0.73	0.476
IL-6	1.21±0.79	0.81±0.64	0.681
IL-12A	1.36±0.85	0.64±0.77	0.443
VEGFA	0.71±0.52	1.29±0.66	0.541
TGFB1	1.46±0.48	0.54±0.48	0.314

Data were expressed as mean ± standard error of the mean (SEM). One-way ANOVA was used for statistical analysis.

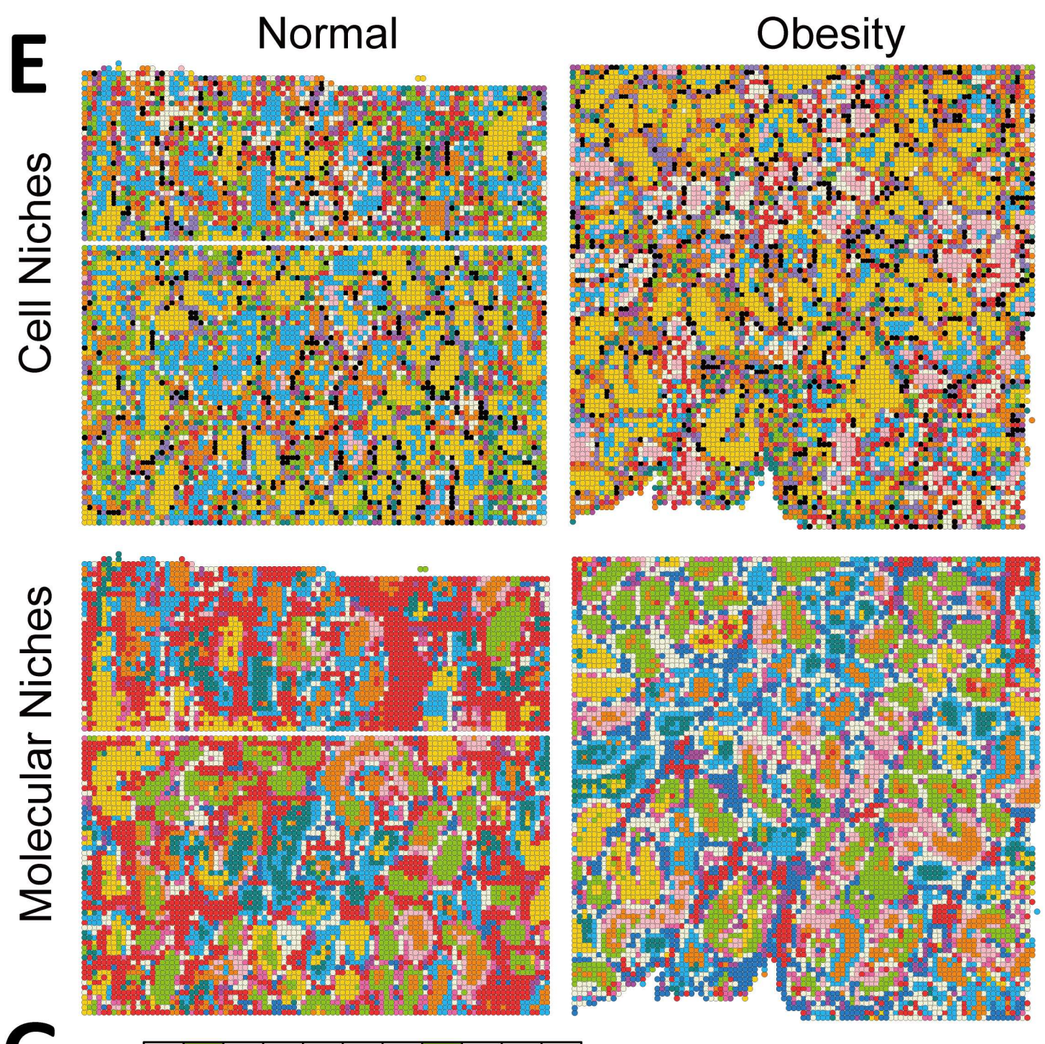

A
Normal (n=3)
Obesity (n=3)
Fresh
Frozen
Single-cell sequence
A1 A2 A3...A96
B1 B2 B3...B96
Spatial transcriptomics
Bioinformatic analysis
B
Elongated
Elongating
LCs & ECs
Macrophage
Round
Sertoli
SPCs
SPGs
UMAP-2
UMAP-1
LCs
ILCs
Myoid
Endothelial
C
SPGs
SPCs
Round
Elongating
Elongated
Sertoli
Macrophage
Myoid
LCs
ILCs
Endothelial
NANOS3
KIT
SPATA22
AURKA
ACRV1
NME5
TNP2
PRSS37
OAZ3
PRM2
SOX9
CLDN11
C1QA
CD14
ACTA2
MYH11
PDGFRA
AR
FLT4
CYP26B1
CD34
COL1A1
Mean expression (gene z-score)
2.5
0
-2.5
Expressing cells (%)
25
50
75
100
Spatial transcriptomics
D
SPGs
Elongating
Round
Myoid
SPCs
Macrophage
Endothelial
Sertoli
LCs
Elongated
ILCs
Shared scale
0.1
0.2
0.3
E
Main Celltype
Elongated
Elongating
Endothelial
ILCs
LCs
Macrophage
Myoid
Round
Sertoli
SPCs
SPGs
0.25
0.50
0.75
F
Spermatogenics
Non-spermatogenics

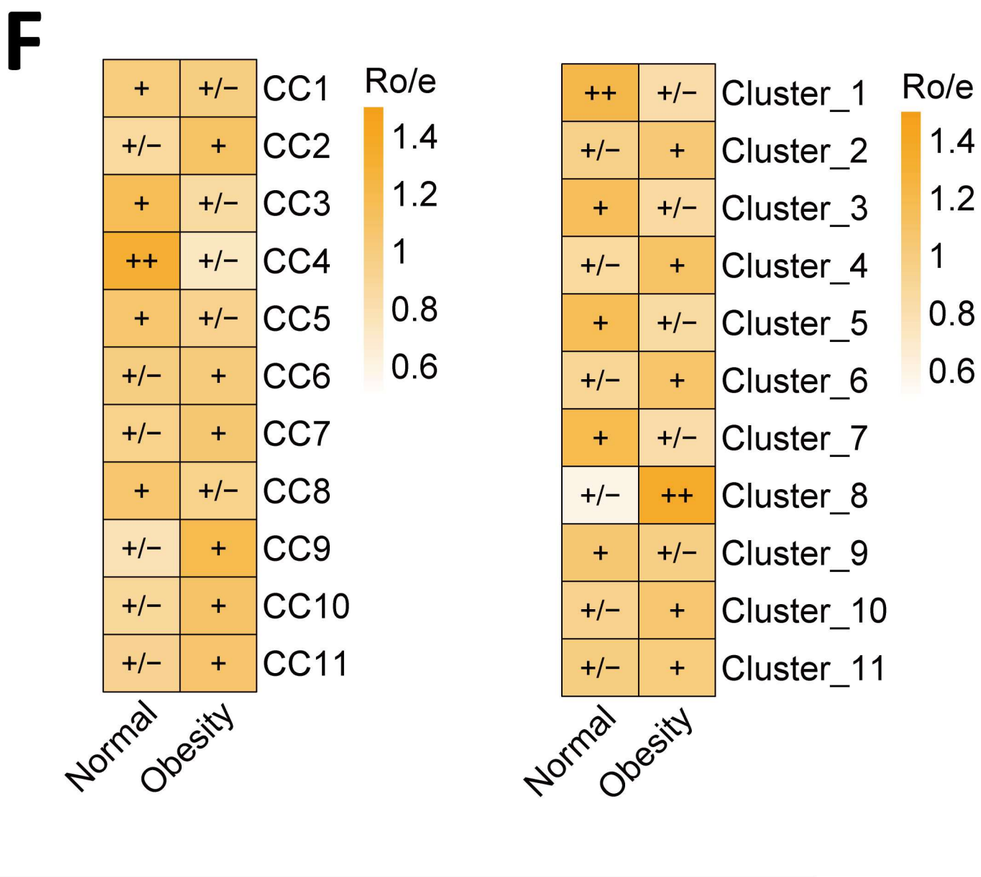

A
Ratio
1.00
0.75
0.50
0.25
0.00
Normal Obesity
0.8
0.6
0.4
0.2
0.0
Normal Obesity
0.25
0.20
0.15
0.10
0.05
0.00
Normal Obesity
Non_Spermatogenics
Spermatogenics
SPGs
SPCs
Round
Elongating
Elongated
Endothelial
ILCs
LCs
Macrophage
Myoid
Sertoli

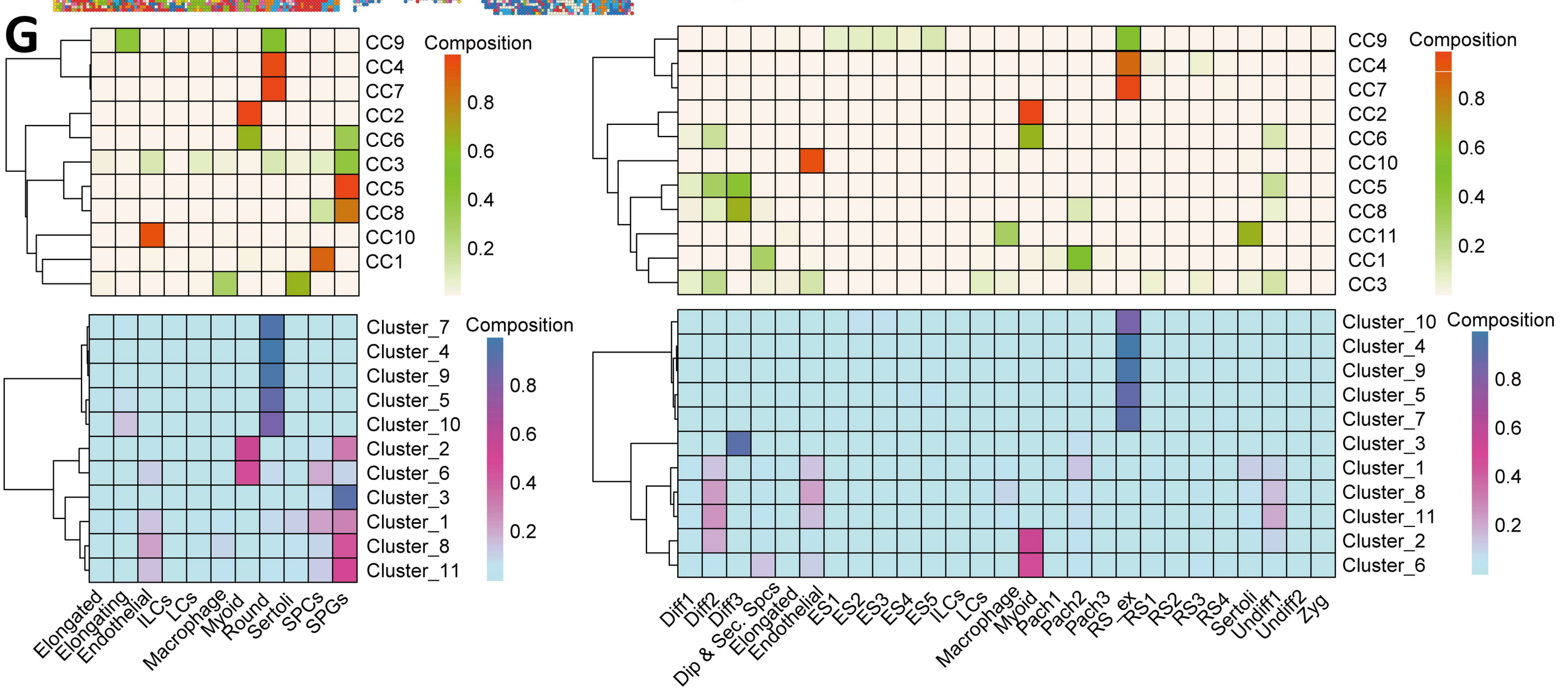

B
SPGs
p = 0.3
SPCs
p = 0.55
Round
p = 0.002
Elongating
p = 0.04
Elongated
p = 0.85
Sertoli
p = 0.07
Macrophage
p = 0.02
Myoid
p = 0.03
Endothelial
p = 0.03
ILCs
p = 0.01
LCs
p = 0.19
Ratio
Normal Obesity

C
SPGs
SPCs
Round
Elongating
Elongated
Sertoli
Macrophage
Myoid
Endothelial
ILCs
LCs
Ro/e
1.4
1.2
1
0.8
0.6
Normal
Obesity

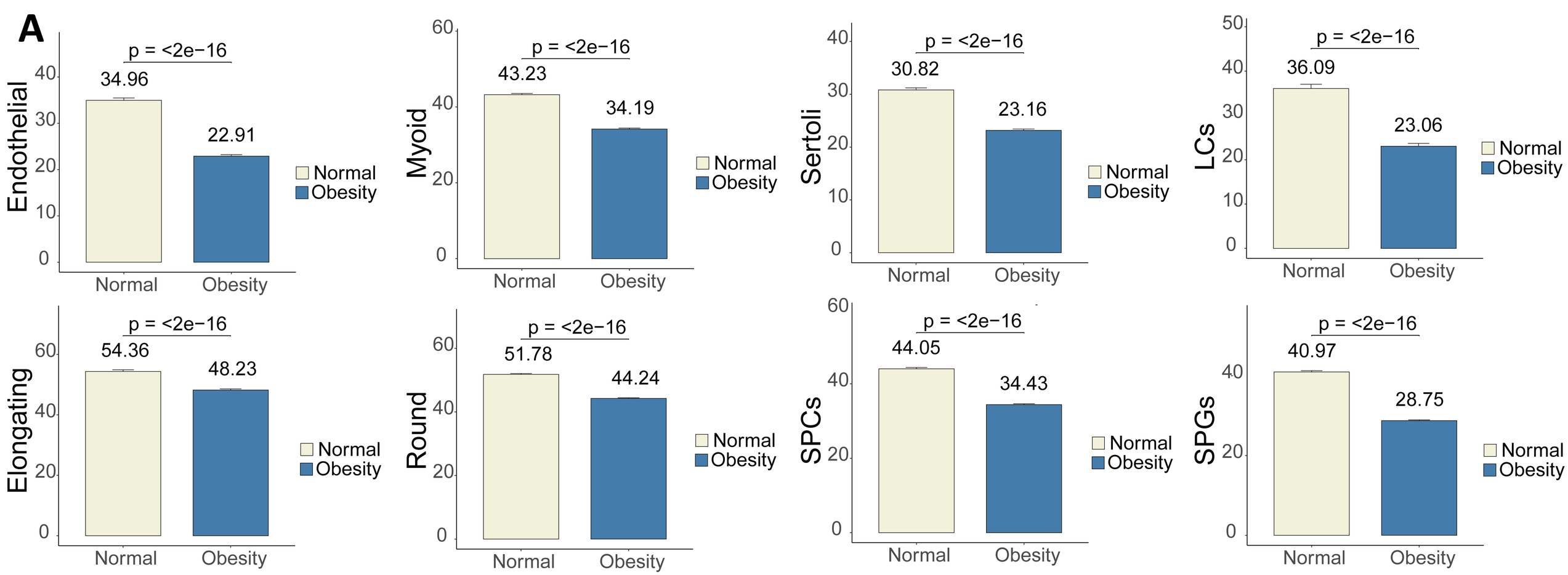
D
Normal
Obesity


E
Normal
Obesity
Cell Niches
Molecular Niches
Composition Clusters
CC1
CC10
CC11
CC2
CC3
CC4
CC5
CC6
CC7
CC8
CC9
Molecular Clusters
Cluster_1
Cluster_10
Cluster_11
Cluster_2
Cluster_3
Cluster_4
Cluster_5
Cluster_6
Cluster_7
Cluster_8
Cluster_9

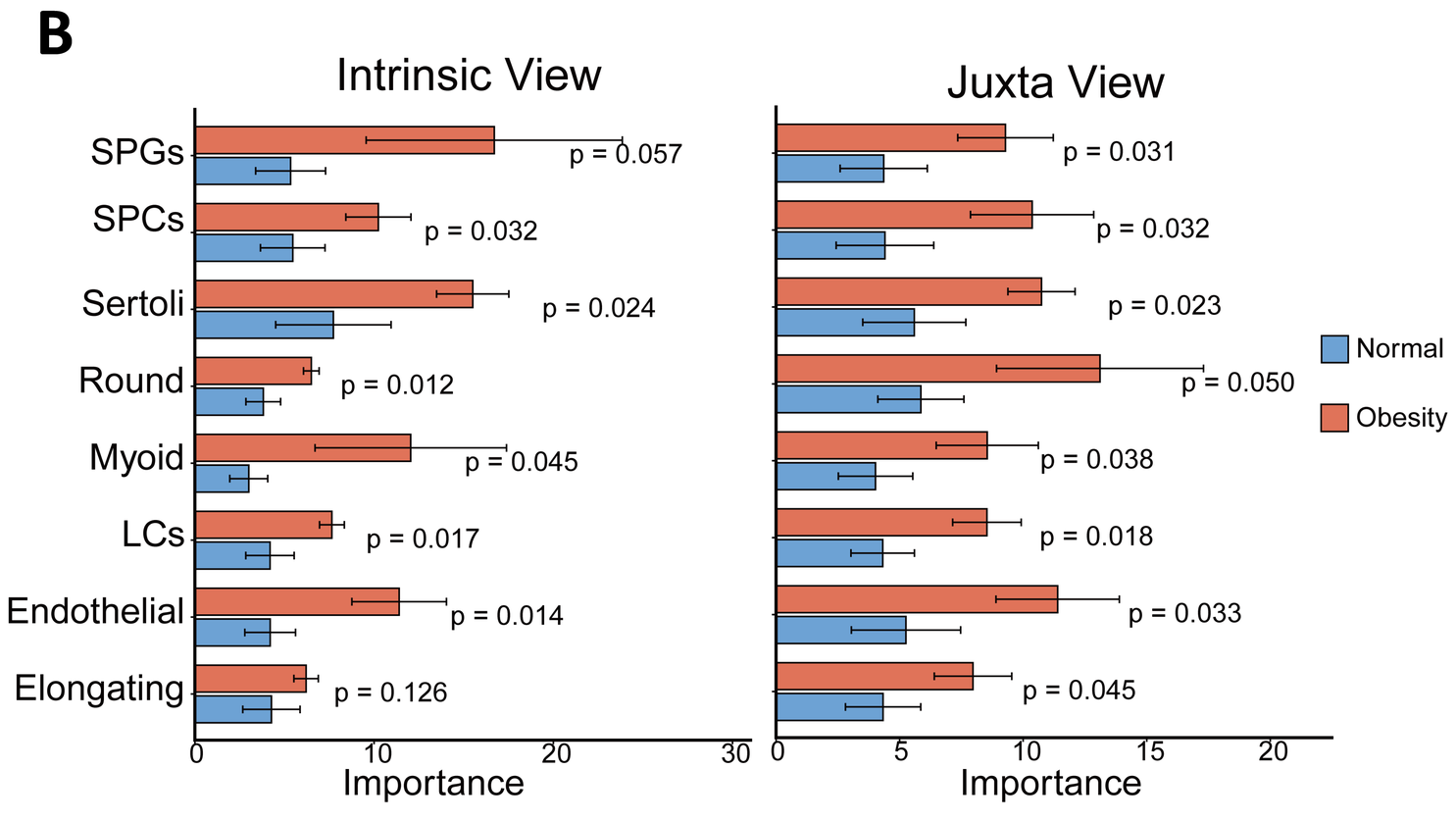

F
CC1
CC2
CC3
CC4
CC5
CC6
CC7
CC8
CC9
CC10
CC11
Ro/e
1.4
1.2
1
0.8
0.6
Normal
Obesity
Cluster_1
Cluster_2
Cluster_3
Cluster_4
Cluster_5
Cluster_6
Cluster_7
Cluster_8
Cluster_9
Cluster_10
Cluster_11


G
CC9
CC4
CC7
CC2
CC6
CC3
CC5
CC8
CC10
CC1
Composition
0.8
0.6
0.4
0.2
Cluster_7
Cluster_4
Cluster_9
Cluster_5
Cluster_10
Cluster_2
Cluster_6
Cluster_3
Cluster_1
Cluster_8
Cluster_11
Elongated
Elongating
Endothelial
ILCs
LCs
Macrophage
Myoid
Round
Sertoli
SPCs
SPGs
Cluster_10
Cluster_4
Cluster_9
Cluster_5
Cluster_7
Cluster_3
Cluster_1
Cluster_8
Cluster_11
Cluster_2
Cluster_6
Diff1
Diff2
Diff3
Dip & Sec. Spcs
Elongated
Endothelial
ES1
ES2
ES3
ES4
ES5
ILCs
LCs
Macrophage
Myoid
Pach1
Pach2
Pach3
RS_ex
RS1
RS2
RS3
RS4
Sertoli
Undiff1
Undiff2
Zyg

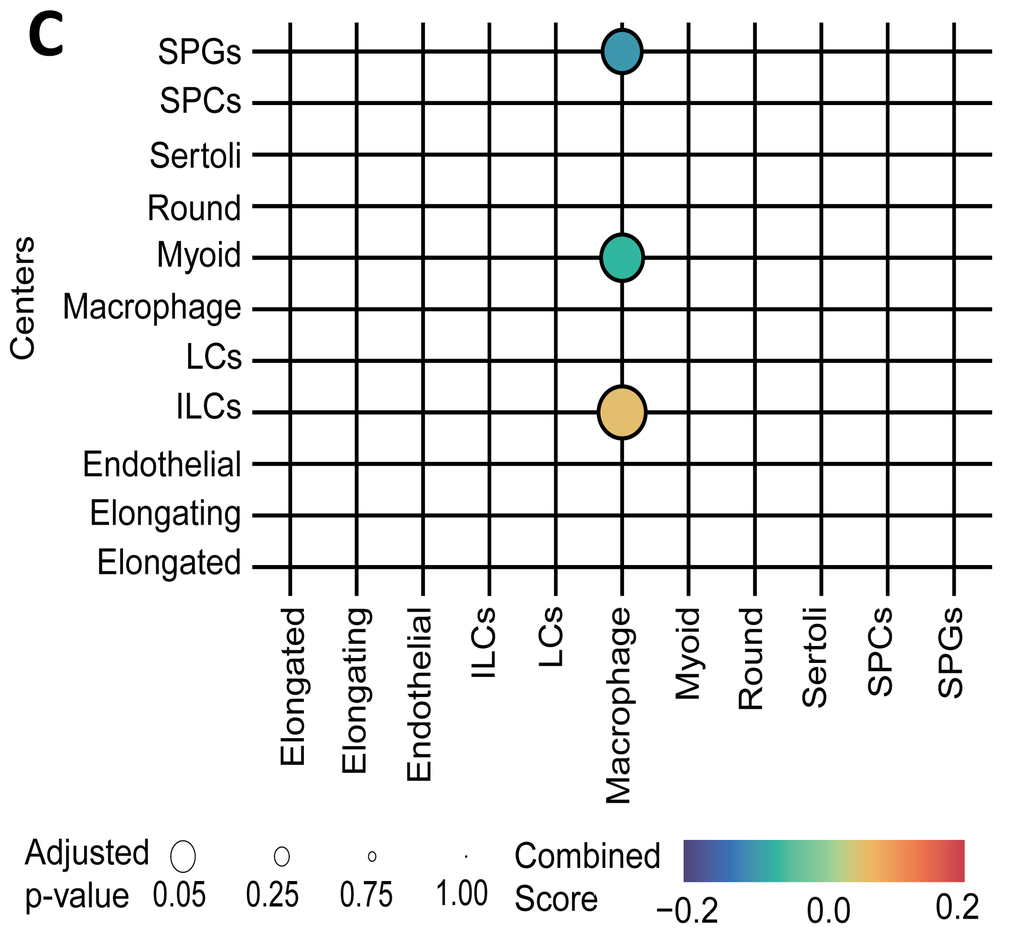
A


Endothelial
p = <2e−16
34.96
22.91
Myoid
p = <2e−16
43.23
34.19
Sertoli
p = <2e−16
30.82
23.16
LCs
p = <2e−16
36.09
23.06
Elongating
p = <2e−16
54.36
48.23
Round
p = <2e−16
51.78
44.24
SPCs
p = <2e−16
44.05
34.43
SPGs
p = <2e−16
40.97
28.75
Normal
Obesity

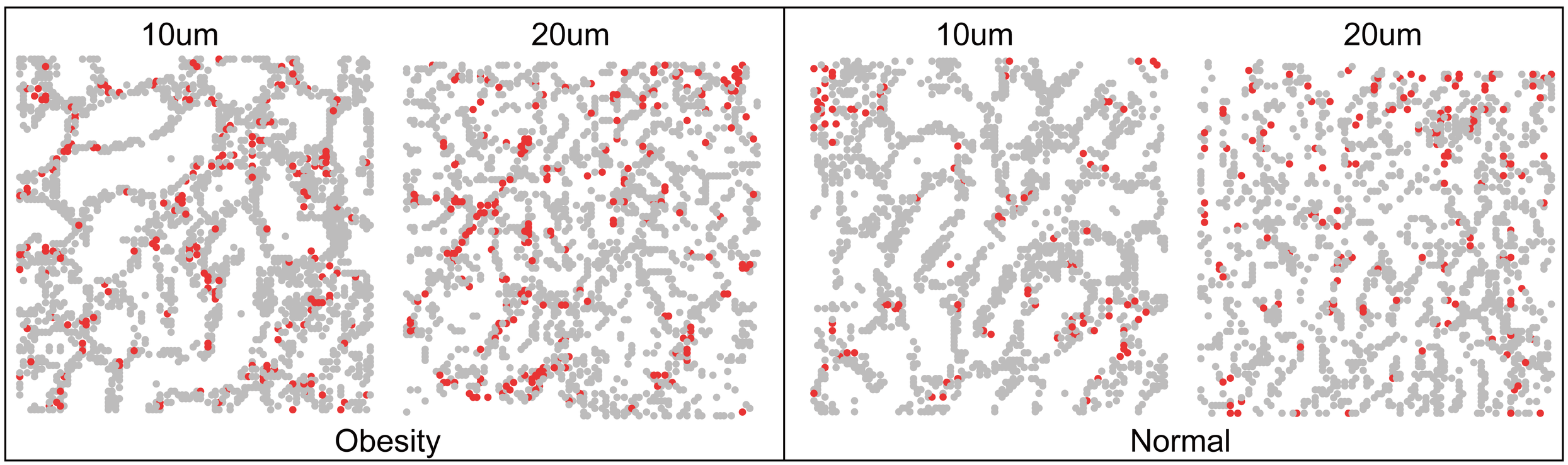
B

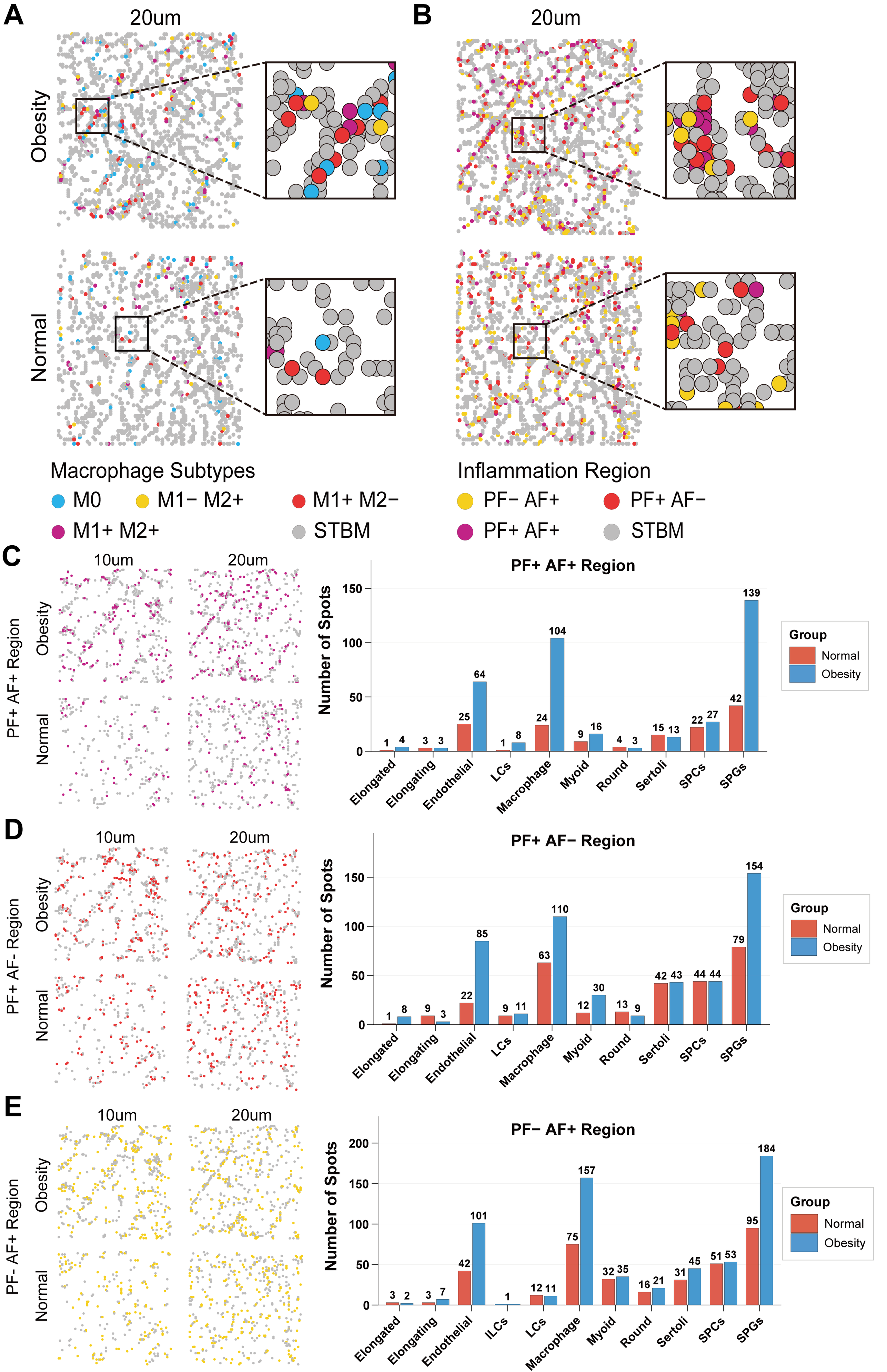

Intrinsic View
Juxta View
SPGs
SPCs
Sertoli
Round
Myoid
LCs
Endothelial
Elongating
p = 0.057
p = 0.032
p = 0.024
p = 0.012
p = 0.045
p = 0.017
p = 0.014
p = 0.126
p = 0.031
p = 0.032
p = 0.023
p = 0.050
p = 0.038
p = 0.018
p = 0.033
p = 0.045
Normal
Obesity
Importance
Importance

C


Centers
SPGs
SPCs
Sertoli
Round
Myoid
Macrophage
LCs
ILCs
Endothelial
Elongating
Elongated
Adjusted p-value
0.05
0.25
0.75
1.00
Combined Score
−0.2
0.0
0.2

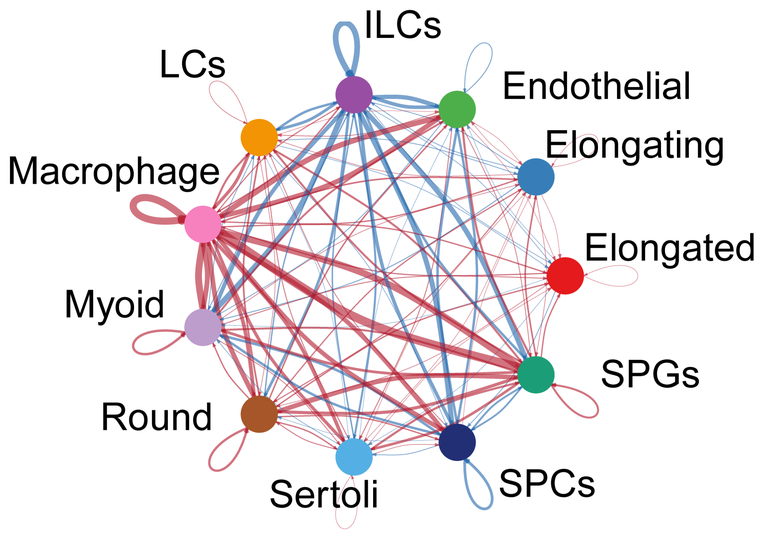
D


10um
20um
10um
20um
Obesity
Normal
Macrophage
STBM

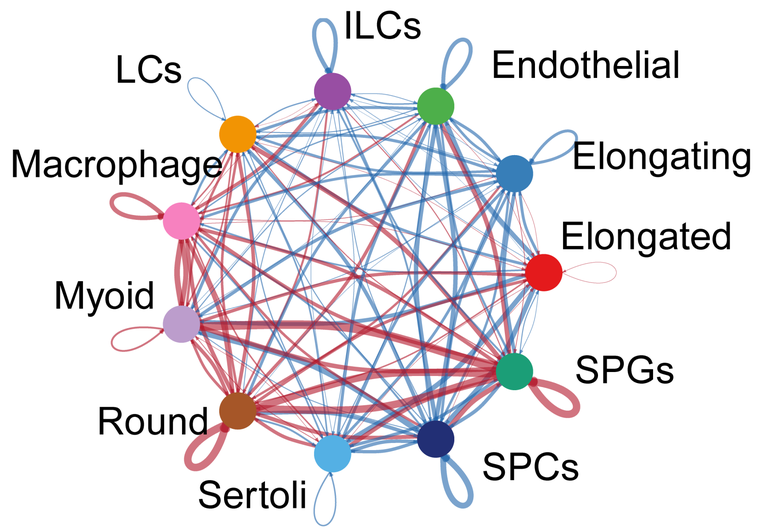

A
20um
Obesity
Normal
B
20um
Macrophage Subtypes
M0
M1− M2+
M1+ M2−
M1+ M2+
STBM
Inflammation Region
PF− AF+
PF+ AF−
PF+ AF+
STBM
C
10um
20um
PF+ AF+ Region
Obesity
Normal
PF+ AF+ Region
Number of Spots
Elongated 1 4
Elongating 3 3
Endothelial 25 64
LCs 1 8
Macrophage 24 104
Myoid 9 16
Round 4 3
Sertoli 15 13
SPCs 22 27
SPGs 42 139
Group
Normal
Obesity
D
10um
20um
PF+ AF- Region
Obesity
Normal
PF+ AF− Region
Number of Spots
Elongated 1 8
Elongating 9 3
Endothelial 22 85
LCs 9 11
Macrophage 63 110
Myoid 12 30
Round 13 9
Sertoli 42 43
SPCs 44 44
SPGs 79 154
Group
Normal
Obesity
E
10um
20um
PF- AF+ Region
Obesity
Normal
PF− AF+ Region
Number of Spots
Elongated 3 2
Elongating 3 7
Endothelial 42 101
ILCs 1
LCs 12 11
Macrophage 75 157
Myoid 32 35
Round 16 21
Sertoli 31 45
SPCs 51 53
SPGs 95 184
Group
Normal
Obesity

A

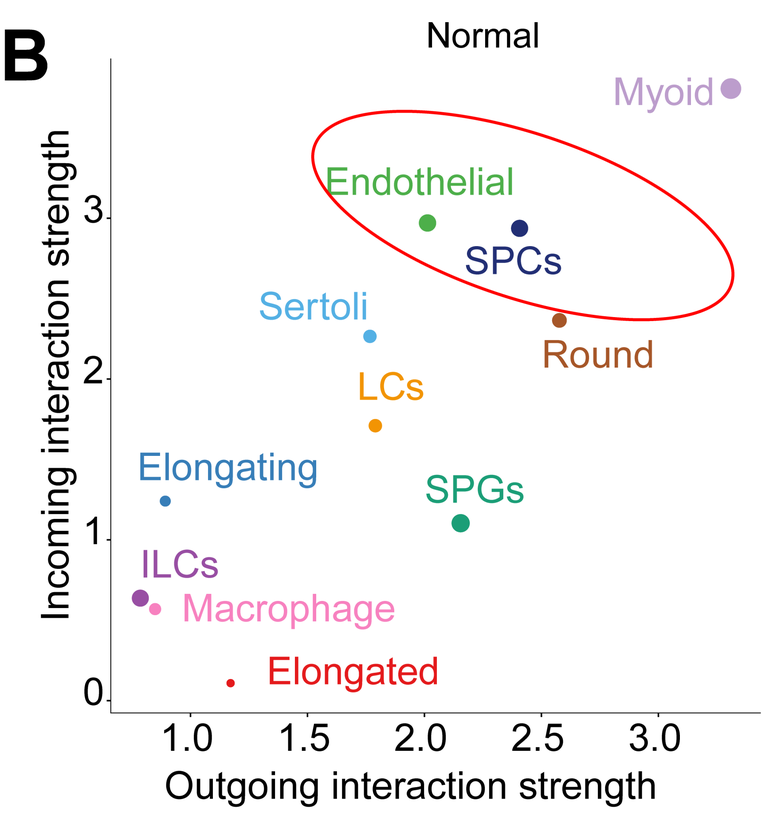
Number

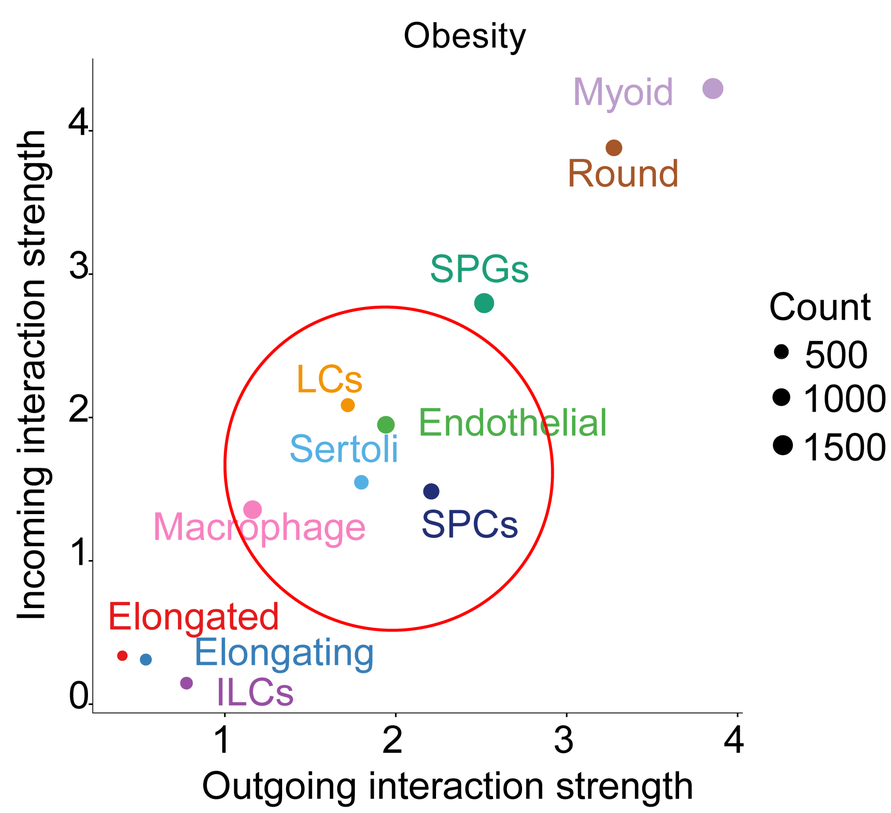


Strength

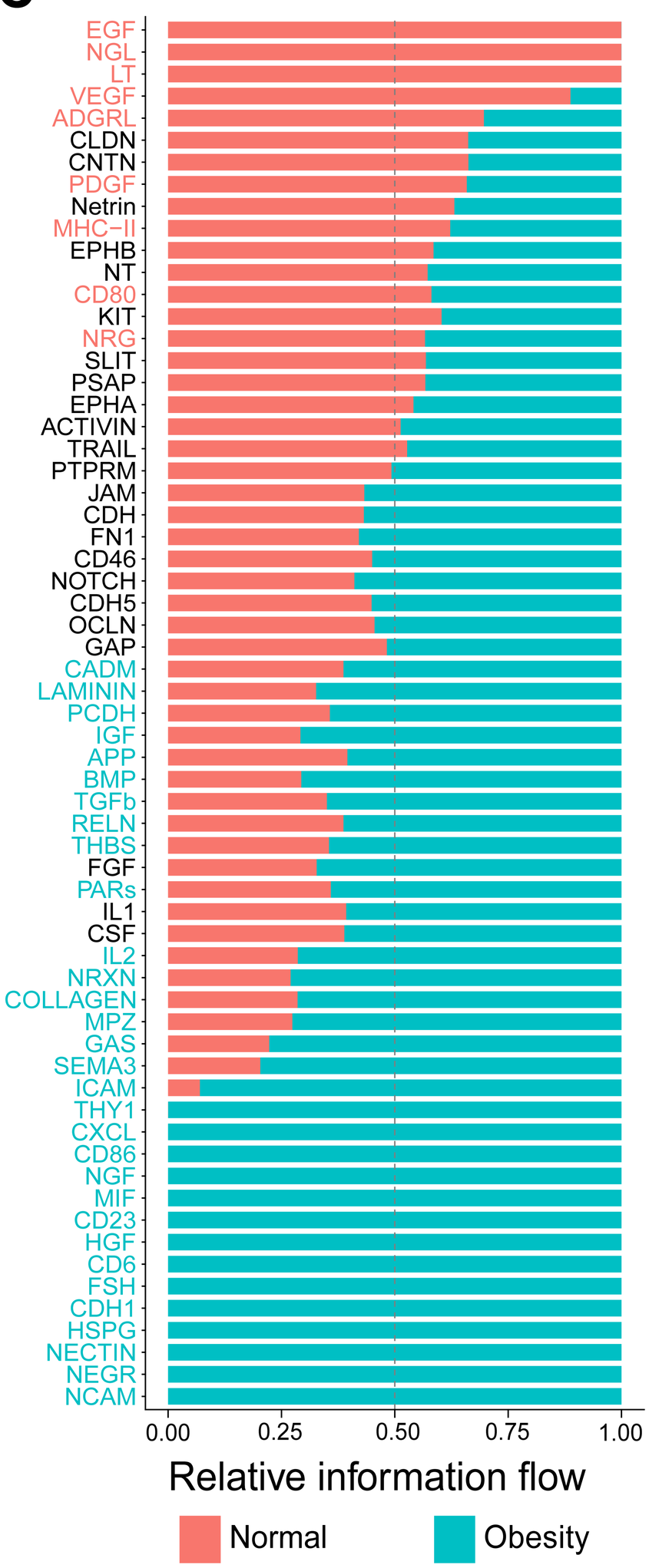


B

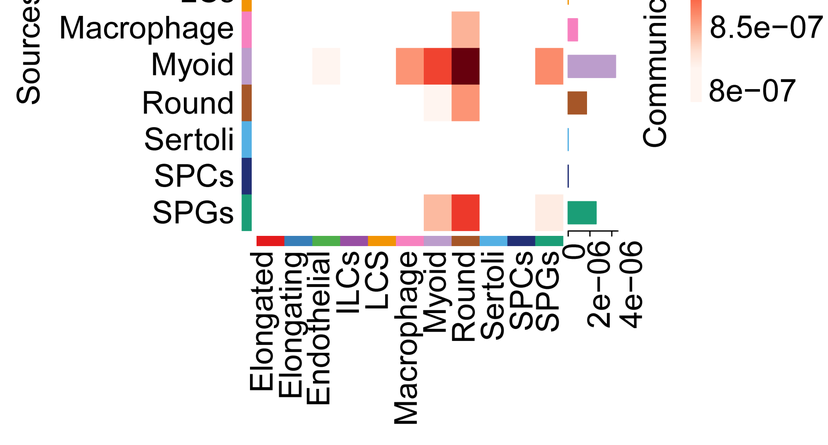


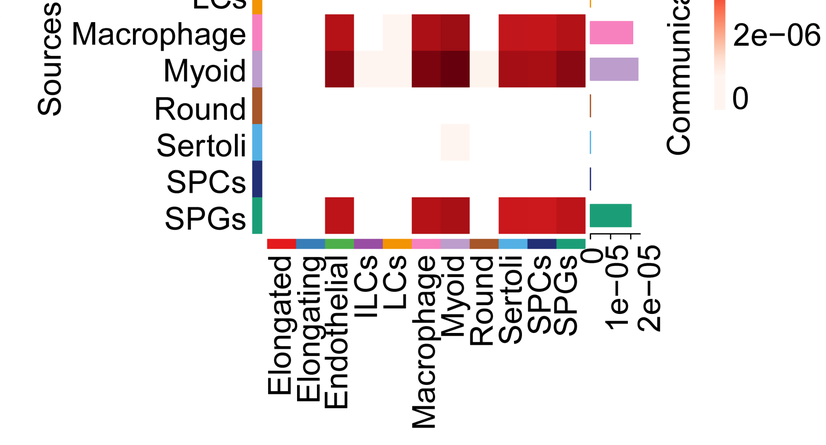


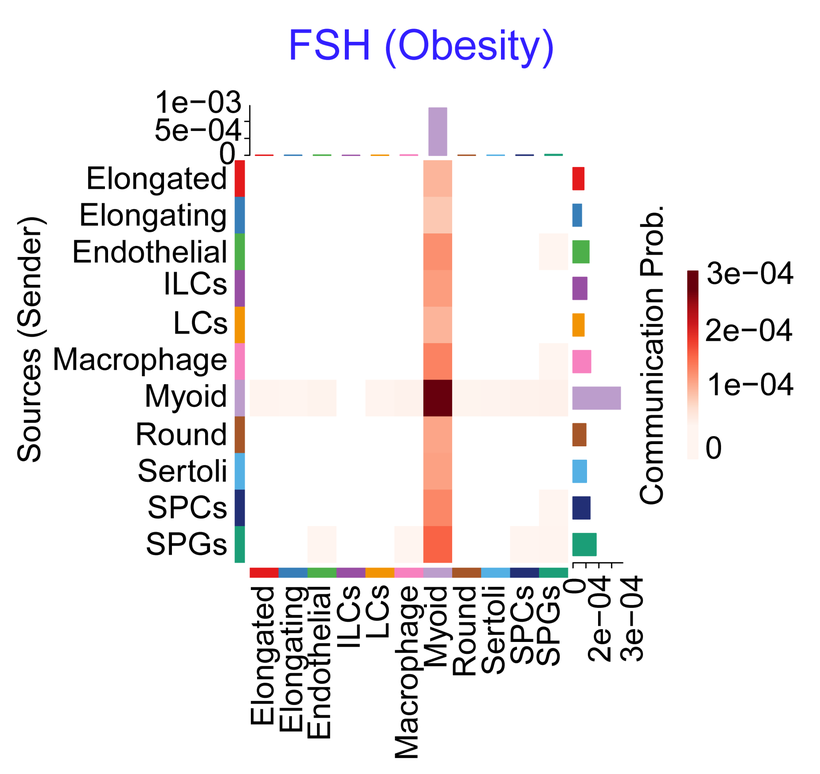
C

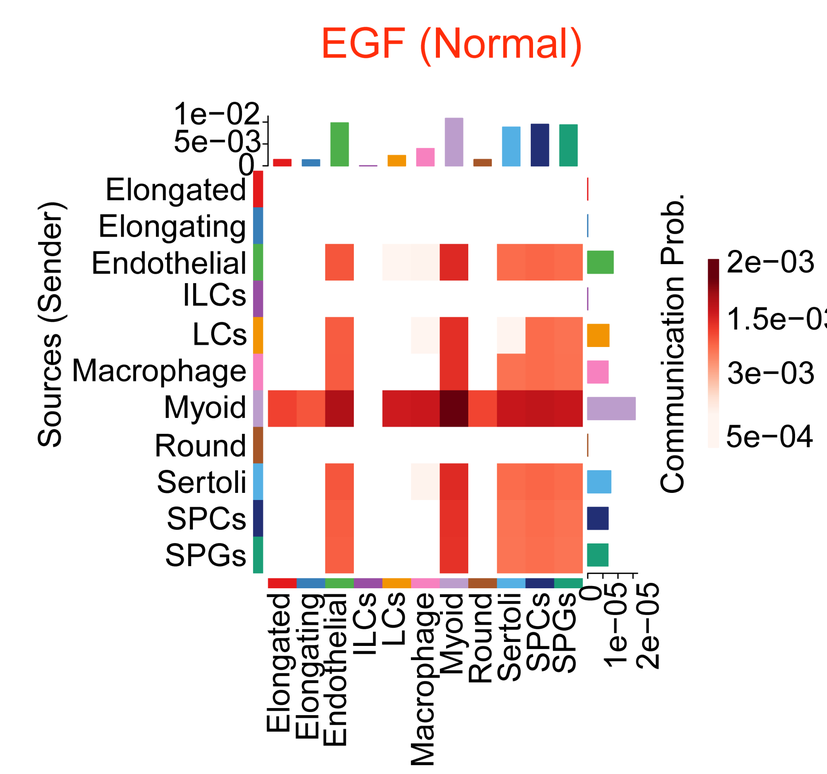


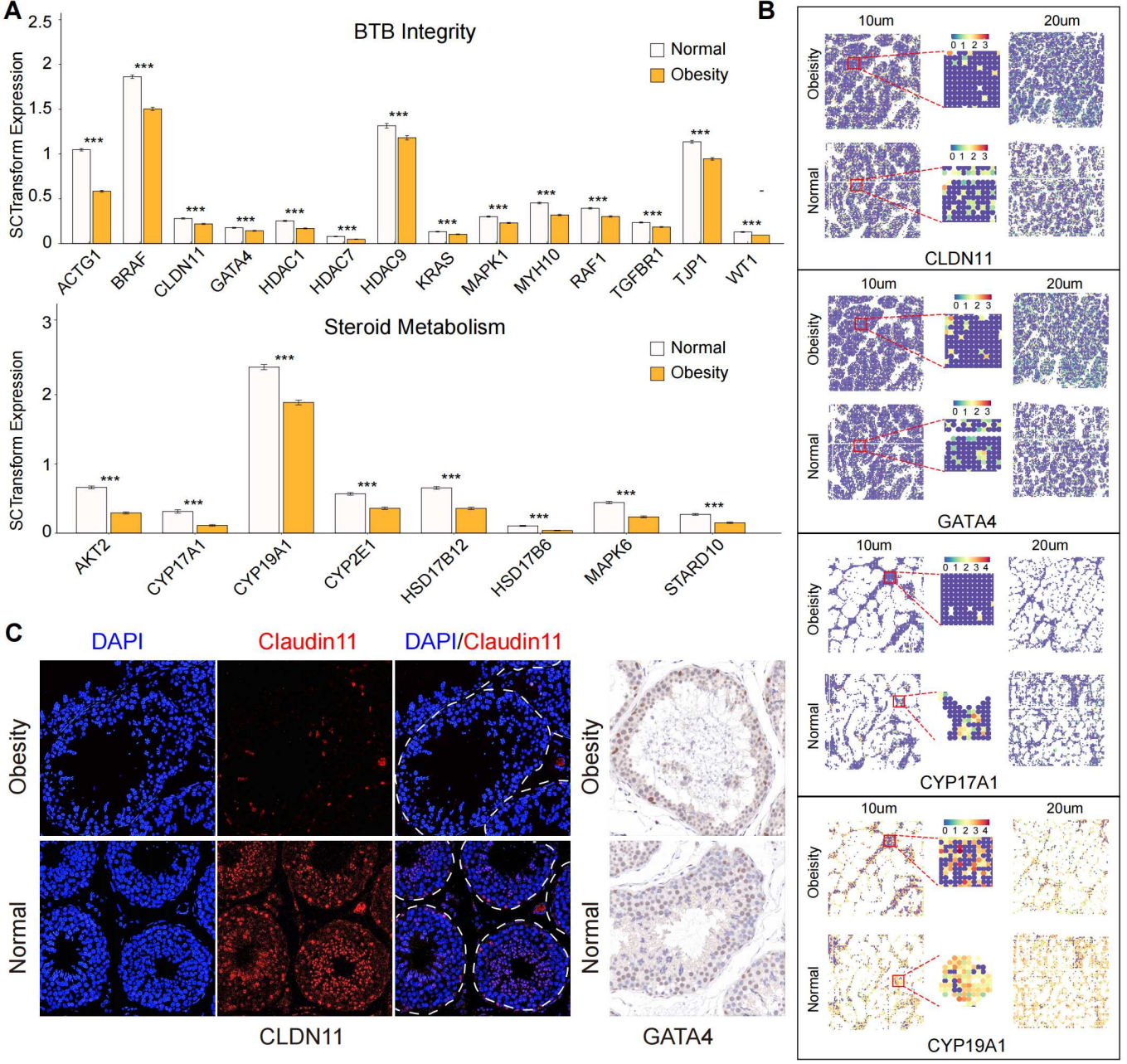
D

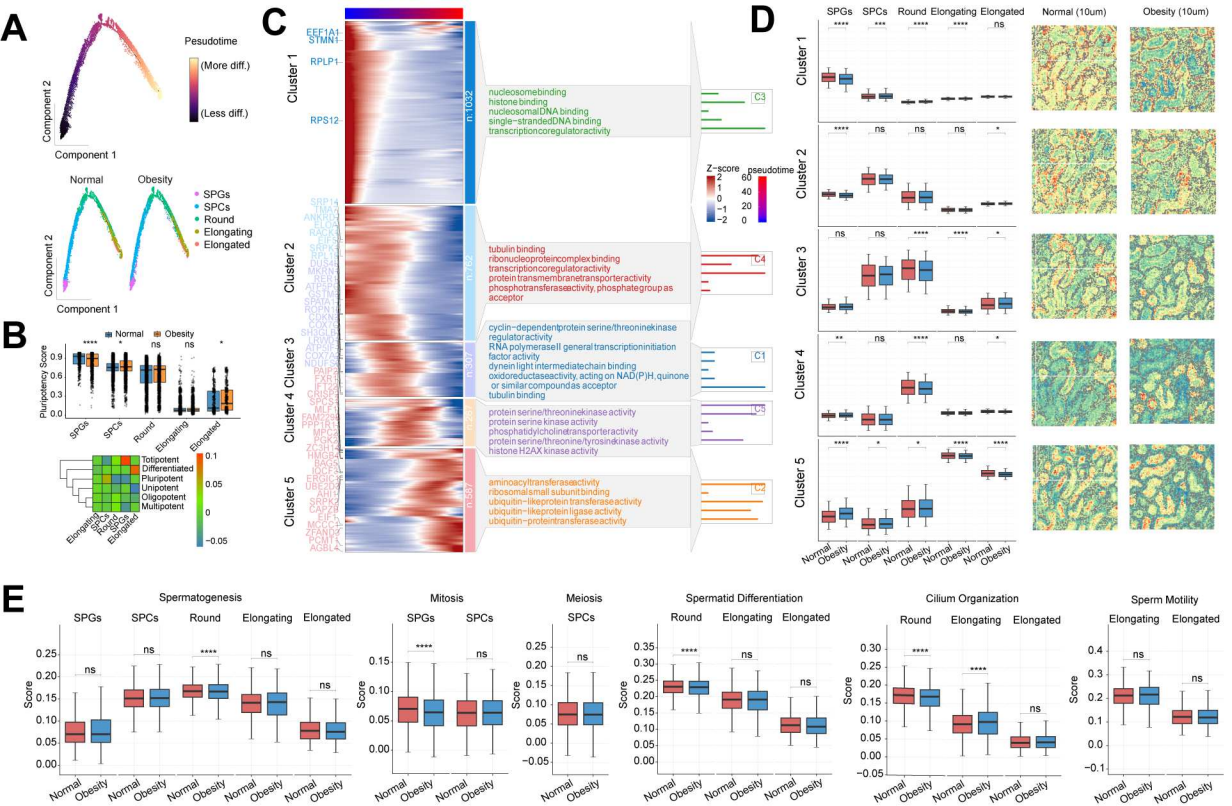




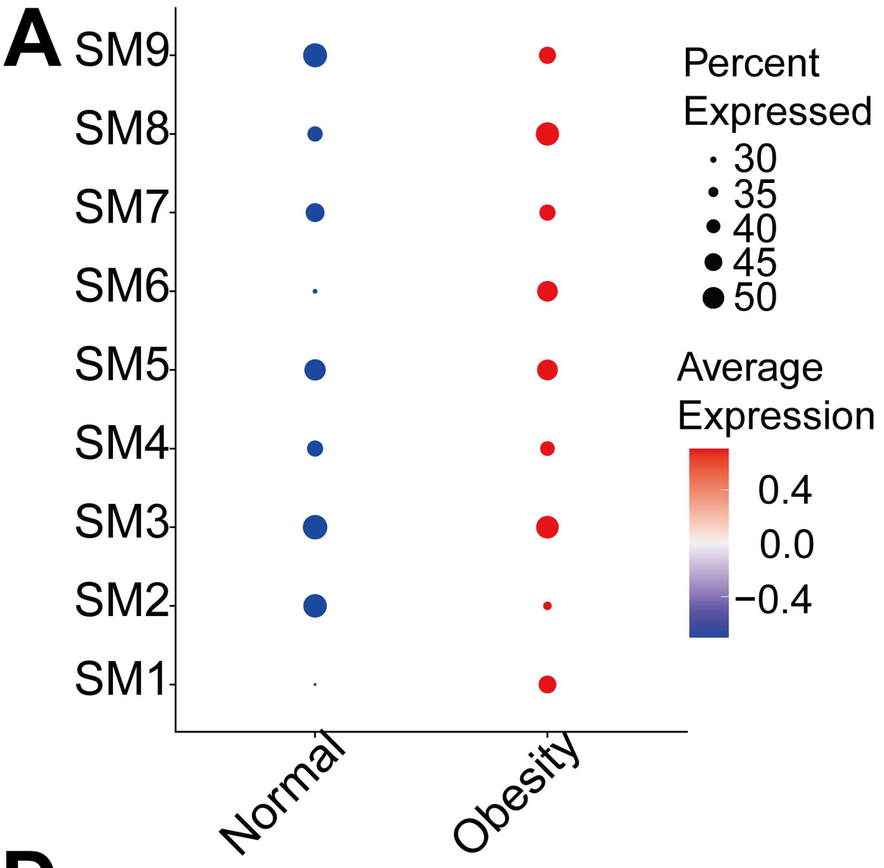




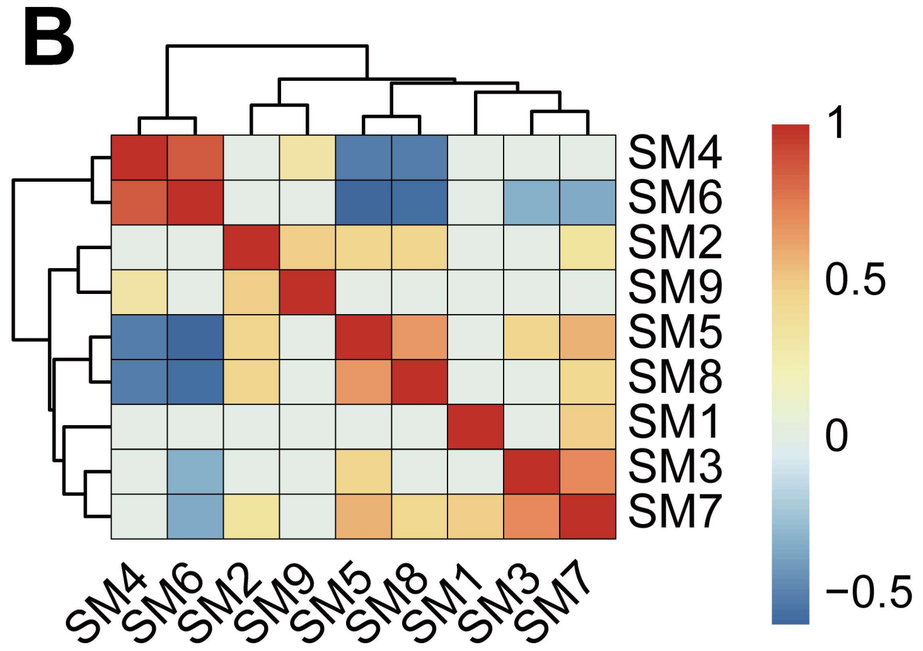

A
BTB Integrity
Normal
Obesity
SCTransform Expression
ACTG1
BRAF
CLDN11
GATA4
HDAC1
HDAC7
HDAC9
KRAS
MAPK1
MYH10
RAF1
TGFBR1
TJP1
WT1
Steroid Metabolism
AKT2
CYP17A1
CYP19A1
CYP2E1
HSD17B12
HSD17B6
MAPK6
STARD10
B
10um
20um
Obesity
Normal
CLDN11
GATA4
CYP17A1
CYP19A1
C
DAPI
Claudin11
DAPI/Claudin11
CLDN11
GATA4


A
Pesudotime
(More diff.)
(Less diff.)
Component 2
Component 1
Normal
Obesity
SPGs
SPCs
Round
Elongating
Elongated
B
Normal
Obesity
Pluripotency Score
SPGs
SPCs
Round
Elongating
Elongated
Totipotent
Differentiated
Pluripotent
Unipotent
Oligopotent
Multipotent
C
Cluster 1
Cluster 2
Cluster 3
Cluster 4
Cluster 5
n.1032
n.1454
n.1007
n.1005
n.1857
nucleosomebinding
histone binding
nucleosomalDNA binding
single−strandedDNA binding
transcriptioncoregulatoractivity
tubulin binding
ribonucleoproteincomplex binding
transcriptioncoregulatoractivity
protein transmembranetransporteractivity
phosphotransferaseactivity, phosphategroup as acceptor
cyclin−dependentprotein serine/threoninekinase regulatoractivity
RNA polymeraseII general transcriptioninitiation factor activity
dynein light intermediatechain binding
oxidoreductaseactivity, acting on NAD(P)H, quinone or similar compound as acceptor
tubulin binding
protein serine/threoninekinase activity
protein serine kinase activity
phosphatidylcholinetransporteractivity
protein serine/threonine/tyrosinekinase activity
histone H2AX kinase activity
aminoacyltransferaseactivity
ribosomal small subunit binding
ubiquitin−likeprotein transferaseactivity
ubiquitin−likeprotein ligase activity
ubiquitin−proteintransferaseactivity
Z−score
pseudotime
D
SPGs
SPCs
Round
Elongating
Elongated
Normal (10um)
Obesity (10um)
Cluster 1
Cluster 2
Cluster 3
Cluster 4
Cluster 5
Normal
Obesity
E
Spermatogenesis
Mitosis
Meiosis
Spermatid Differentiation
Cilium Organization
Sperm Motility
Score

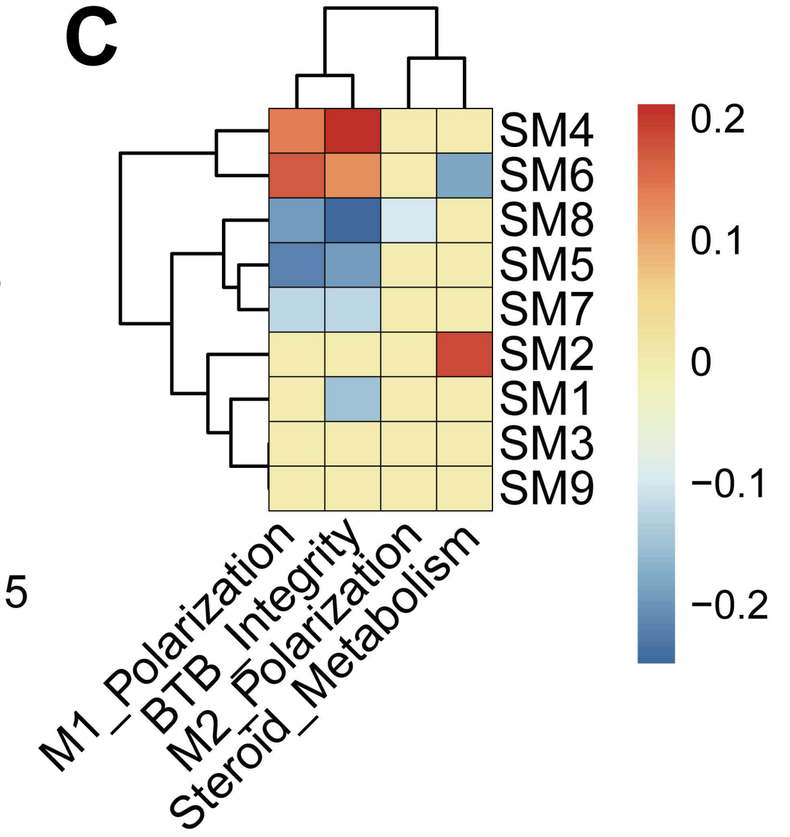
A


SM9
SM8
SM7
SM6
SM5
SM4
SM3
SM2
SM1
Normal
Obesity
Percent Expressed
30
35
40
45
50
Average Expression
0.4
0.0
−0.4

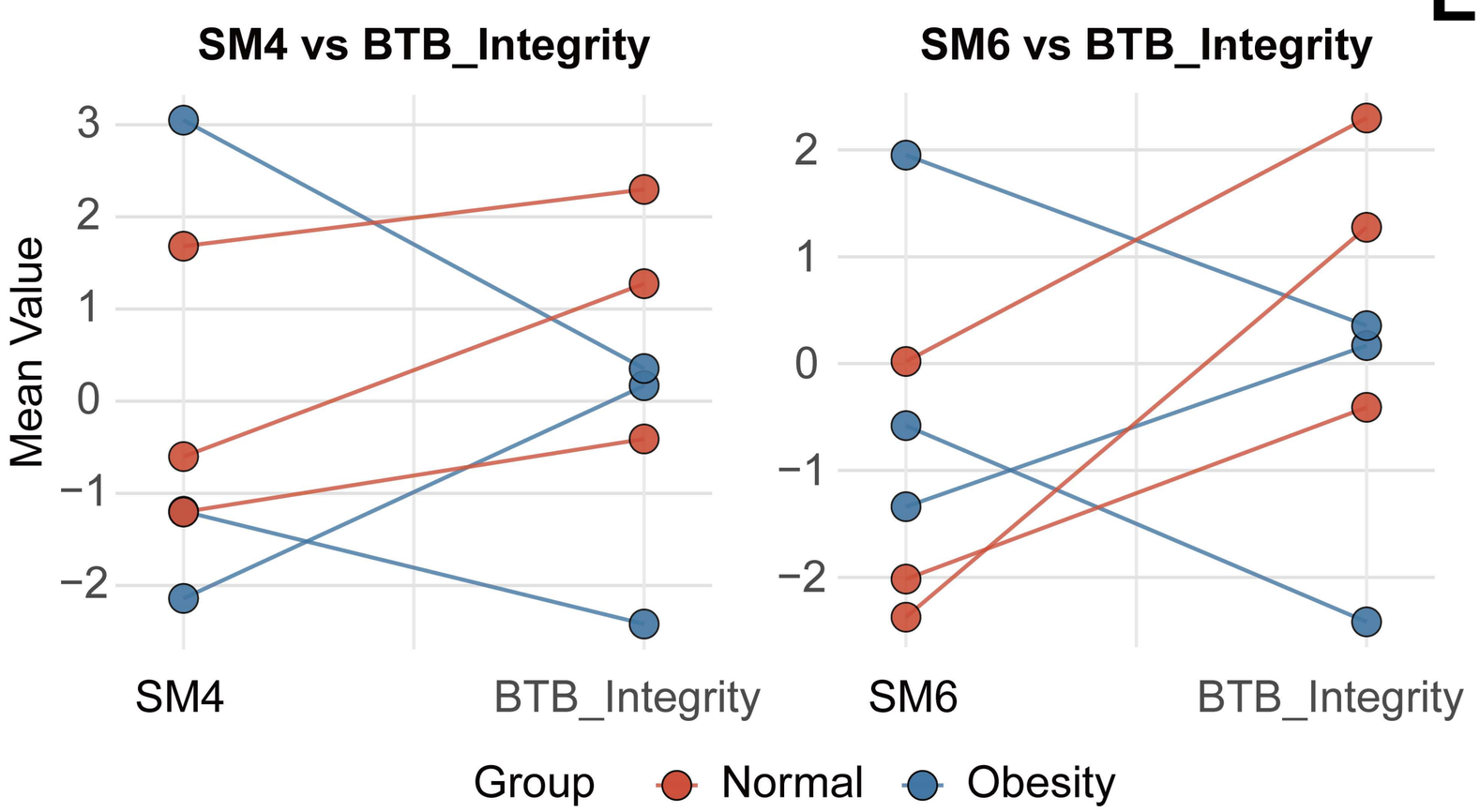
B


SM4
SM6
SM2
SM9
SM5
SM8
SM1
SM3
SM7
1
0.5
0
−0.5

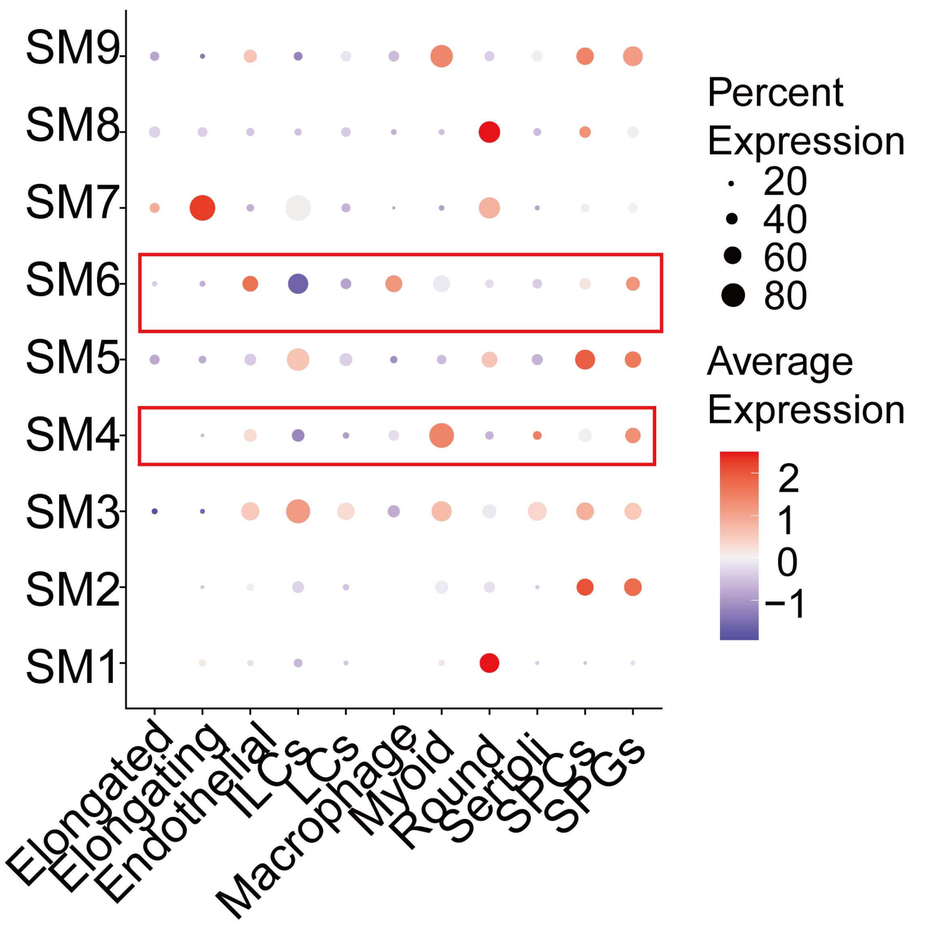
C


SM4
SM6
SM8
SM5
SM7
SM2
SM1
SM3
SM9
M1_Polarization
BTB_Integrity
M2_Polarization
Steroid_Metabolism
0.2
0.1
0
−0.1
−0.2

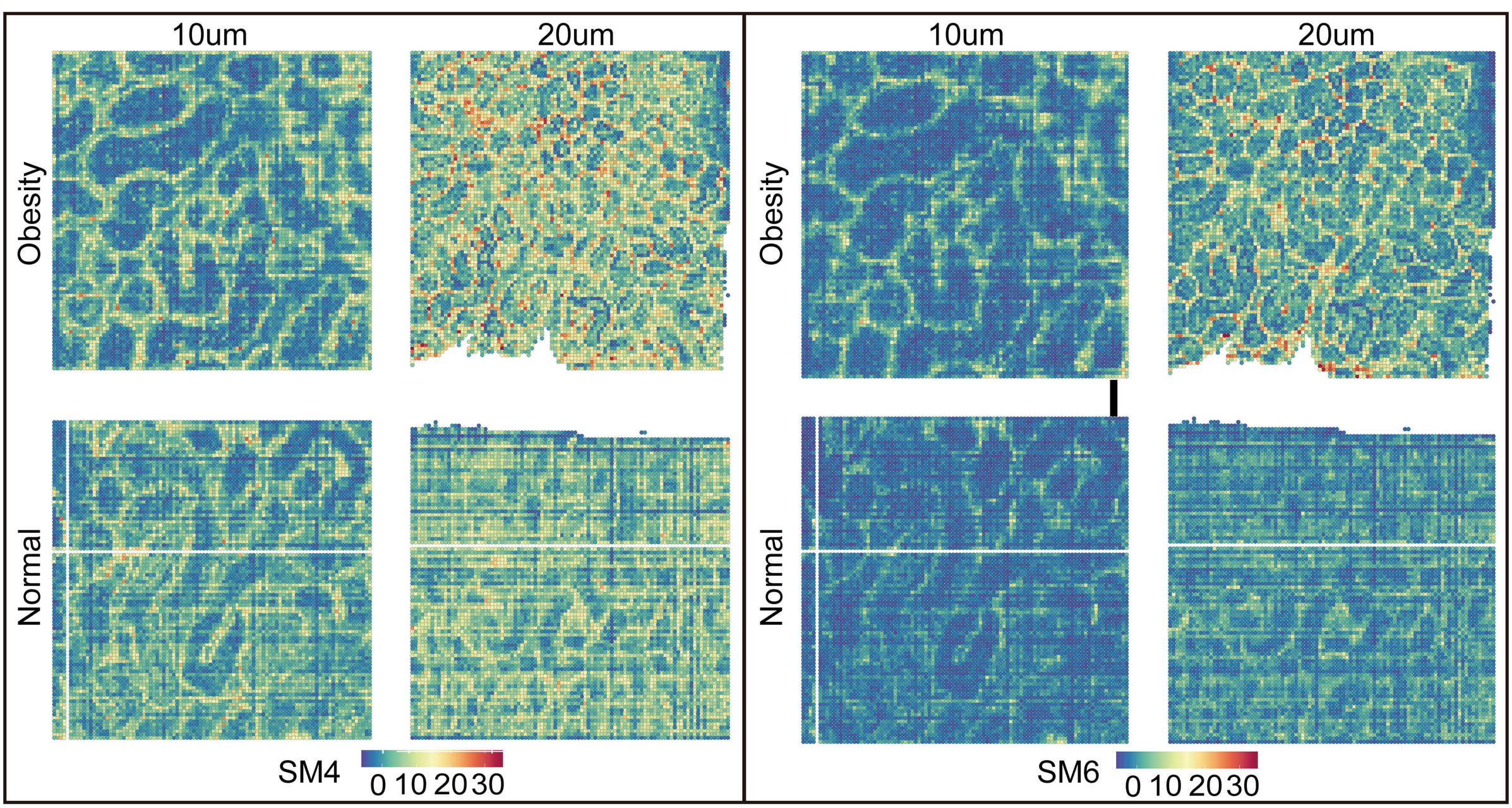
D

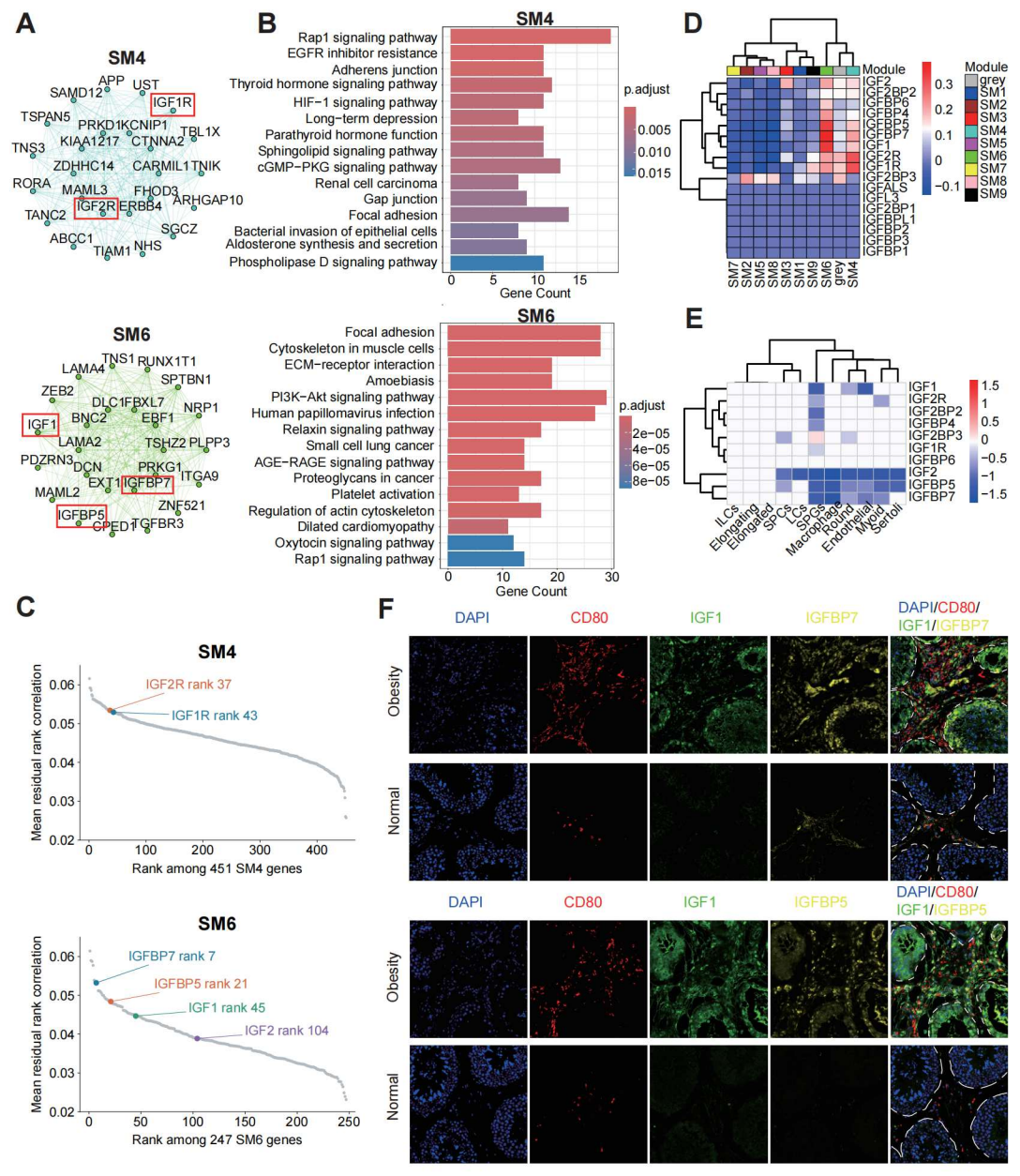

SM4 vs BTB_Integrity
SM6 vs BTB_Integrity
Mean Value
SM4
BTB_Integrity
SM6
BTB_Integrity
Group
Normal
Obesity

E


SM9
SM8
SM7
SM6
SM5
SM4
SM3
SM2
SM1
Elongated
Elongating
Endothelial
ILCs
LCs
Macrophage
Myoid
Round
Sertoli
SPCs
SPGs
Percent Expression
20
40
60
80
Average Expression
2
1
0
−1

F


10um
20um
10um
20um
Obesity
Normal
Obesity
Normal
SM4
0 10 20 30
SM6
0 10 20 30


A
SM4
APP
UST
SAMD12
IGF1R
TSPAN5
PRKD1
KCNIP1
TBL1X
KIAA1217
CTNNA2
TNS3
ZDHHC14
CARMIL1
TNIK
RORA
MAML3
FHOD3
ARHGAP10
IGF2R
ERBB4
TANC2
SGCZ
ABCC1
TIAM1
NHS
SM6
TNS1
RUNX1T1
LAMA4
SPTBN1
ZEB2
DLC1
FBXL7
NRP1
IGF1
BNC2
EBF1
LAMA2
TSHZ2
PLPP3
PDZRN3
DCN
PRKG1
EXT1
IGFBP7
ITGA9
MAML2
ZNF521
IGFBP5
CPED1
TGFBR3
B
SM4
Rap1 signaling pathway
EGFR inhibitor resistance
Adherens junction
Thyroid hormone signaling pathway
HIF−1 signaling pathway
Long−term depression
Parathyroid hormone function
Sphingolipid signaling pathway
cGMP−PKG signaling pathway
Renal cell carcinoma
Gap junction
Focal adhesion
Bacterial invasion of epithelial cells
Aldosterone synthesis and secretion
Phospholipase D signaling pathway
0
5
10
15
Gene Count
p.adjust
0.005
0.010
0.015
SM6
Focal adhesion
Cytoskeleton in muscle cells
ECM−receptor interaction
Amoebiasis
PI3K−Akt signaling pathway
Human papillomavirus infection
Relaxin signaling pathway
Small cell lung cancer
AGE−RAGE signaling pathway
Proteoglycans in cancer
Platelet activation
Regulation of actin cytoskeleton
Dilated cardiomyopathy
Oxytocin signaling pathway
Rap1 signaling pathway
0
10
20
30
Gene Count
p.adjust
2e−05
4e−05
6e−05
8e−05
C
SM4
IGF2R rank 37
IGF1R rank 43
Mean residual rank correlation
0.06
0.05
0.04
0.03
0.02
0
100
200
300
400
Rank among 451 SM4 genes
SM6
IGFBP7 rank 7
IGFBP5 rank 21
IGF1 rank 45
IGF2 rank 104
Mean residual rank correlation
0.06
0.05
0.04
0.03
0.02
0
50
100
150
200
250
Rank among 247 SM6 genes
D
Module
IGF2
IGFBP2
IGFBP6
IGFBP4
IGFBP5
IGFBP7
IGF1
IGF2R
IGF1R
IGF2BP3
IGFALS
IGFL3
IGF2BP1
IGFBPL1
IGFBP2
IGFBP3
IGFBP1
0.3
0.2
0.1
0
−0.1
Module
grey
SM1
SM2
SM3
SM4
SM5
SM6
SM7
SM8
SM9
SM7
SM2
SM5
SM8
SM3
SM1
SM9
SM6
grey
SM4
E
IGF1
IGF2R
IGF2BP2
IGFBP4
IGF2BP3
IGF1R
IGFBP6
IGF2
IGFBP5
IGFBP7
1.5
1
0.5
0
−0.5
−1
−1.5
ILCs
Elongating
Elongated
SPCs
LCs
sPCs
Macrophage
Round
Endothelial
Myoid
Sertoli
F
DAPI
CD80
IGF1
IGFBP7
DAPI/CD80/
IGF1/IGFBP7
Obesity
Normal
DAPI
CD80
IGF1
IGFBP5
DAPI/CD80/
IGF1/IGFBP5
Obesity
Normal

A

Tom Matrix

Combine

TF Network

Condition 1

Condition 2

Condition 3

TF regulation

Correlation

Gene

TF

B

SM4 Type TF Gene

SM6 Type TF Gene

C

SM4

SM6

D

Avg. log2(FC), Negative Regulons

Avg. log2(FC), Positive Regulons

E

Target Module

Source Module

Positive Regulatory Score

F

Target Module

Source Module

Negative Regulatory Score

Supplementary Files

This is a list of supplementary files associated with this preprint. Click to download.

- SupplemenataryFigures.docx
- TableS1.xlsx
- TableS2.xlsx
- TableS3.xlsx